Electronic Properties of Carbon-Based Superatomic Structures

Shuqi Xie, Kun Ni, and Yanwu Zhu**

Carbon-based materials, ranging from traditional allotropes like diamond and graphite to nanostructures such as fullerenes, carbon nanotubes, and graphene, have attracted extensive research attention due to their unique electronic properties and versatile applications. Recently, the concept of superatomic structures, which refers to the assembly of nano units that exhibit collective electronic properties analogous to those of individual atoms, has emerged as an intriguing frontier in carbon research. The exploration of carbon-based superatomic structures opens up new possibilities for designing materials with tailored electronic properties, potentially leading to the development of next-generation electronic devices. In this review, the progress on the electronic properties of carbon-based superatomic structures is briefly summarized, with a focus on the electronic properties of those structures assembled from carbon nanomaterials.

1. Introduction

Research of carbon-based materials has been a hotspot in materials science, ranging from traditional 3D atomic carbons, such as graphite and diamond, to nano carbons, e.g., 0D fullerenes,[1] 1D carbon nanotubes (CNTs),[2] and 2D graphene.[3] Exploring more allotropes like graphdiyne,[4] carbon nanohorns,[5] nano onions,[6] and other nanocarbon materials[7] has enabled carbon-based materials to exhibit diverse electronic features ranging from metallic to semiconducting or insulating. Such diversity originates not only from sp, sp^2, and sp^3 (or mixed) hybridization of carbon atoms but also from the dimensional modulation and curvature introduction to the structures, as schematically shown in **Figure** 1a. In recent years, carbon-based superatomic structures have emerged with the rapid development of carbon materials, bringing new opportunities for breakthroughs in the application of electronic devices.

The concept of superatoms originated from the electronic property investigation of metal clusters, particularly including the discovery of aluminum clusters (e.g., Al_{13}^-) by the Castleman group in 1989[11] Al_{13}^- clusters exhibit atom-like electronic structures characterized by closed-shell configurations in s, p, and d orbitals, resembling the behavior of traditional atoms.[12] To explain the phenomenon of electronic shell closure in such clusters, Matisse et al. introduced the jellium model,[13] which treats the valence electrons of the cluster as moving in a spherical symmetry potential, similar to the situations in an atom. When the number of electrons in the cluster matches the magic number predicted by the jellium model, the cluster demonstrates enhanced stability. Extending this theoretical framework to carbon, Feng et al. identified the presence of superatomic molecular orbitals (SAMOs) in C_{60} molecules through low-temperature scanning tunneling microscopy and density functional theory (DFT) calculations.[14]

In more generalized situations, a "superatomic" carbon crystal refers to a hierarchical structure constructed by using carbon nanostructures as units in a crystal-like periodic arrangement, exhibiting unique electronic properties through artificially designed superlattices and topological features. The SAMOs endow a fullerene cage with atomic-like electronic characteristics;[8] the twisting of layers in bilayer graphene causes unconventional superconductivity observed at a specific "magic angle" between layers.[15] On one hand, the electronic behavior of superatomic structures can be precisely controlled through molecular design,[16] dimensionality control,[17] stacking methods,[18] and external physical field such as electric and magnetic fields,[19] pressure and temperature,[19, 20] showing the high tunability. On the other hand, the study of electronic properties benefits the theoretical development of materials science in carbon research, providing new models and tools for understanding the complex relationship between physical properties and superatomic structures. These characteristics provide a new perspective for understanding the quantum phenomena and lay the foundation for the development of future high-performance electronic devices, where the study of the electronic properties has extremely important scientific significance.

Carbon-based superatomic structures can exhibit broad application potential across multiple fields such as electronic devices, quantum information, and catalysis. C_{60} nanowires used in high-performance field-effect transistors (FETs) can achieve an electron mobility of 11 $cm^2\ V^{-1}\ s^{-1}$ and an on/off current ratio greater than 10^5.[21] High-density semiconducting CNT

S. Xie, K. Ni, Y. Zhu
Department of Materials Science and Engineering
School of Chemistry and Materials Science
Hefei National Research Center for Physical Sciences at the Microscale
& State Key Laboratory of Precision and Intelligent Chemistry
University of Science and Technology of China
Hefei, Anhui 230026, China
E-mail: nikun@ustc.edu.cn; zhuyanwu@ustc.edu.cn

The ORCID identification number(s) for the author(s) of this article can be found under https://doi.org/10.1002/adfm.202508106

DOI: 10.1002/adfm.202508106

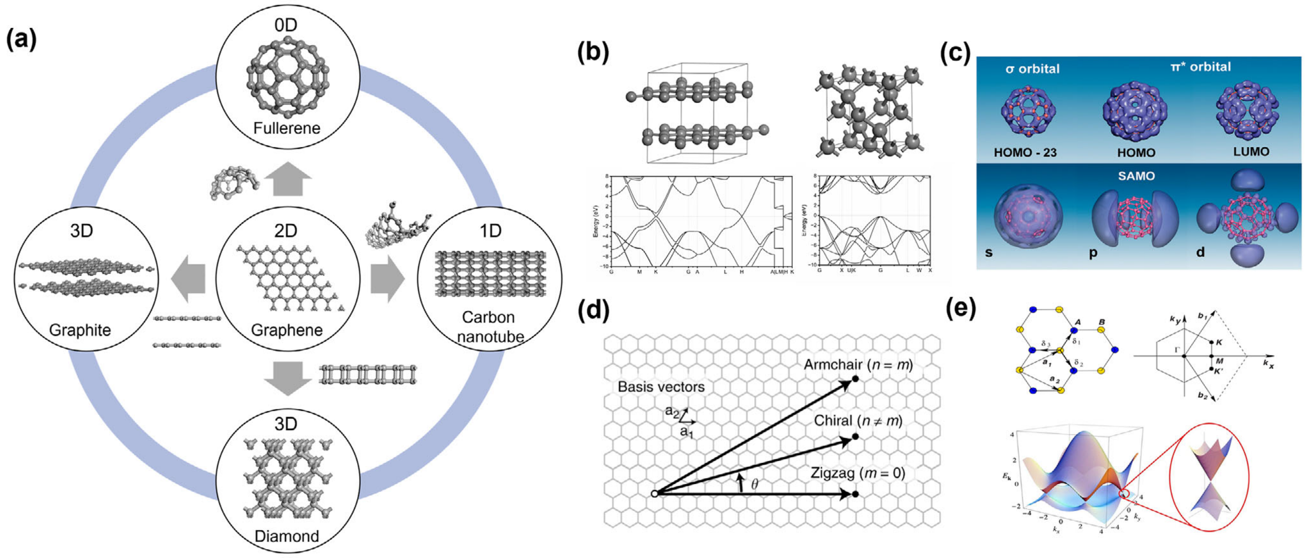

Figure 1. a) Carbon materials with different dimensionalities; b) geometry and electronic band structures of diamond and graphite; c) DFT calculated σ, HOMO, LUMO orbitals, and s, p, d SAMOs states of C_{60}; Reproduced with permission.[8] Copyright 2009, American Chemical Society. d) Schematic illustration of SWNTs formed with different chiral indices (n, m); Reproduced with permission.[9] Copyright 2019, Springer Nature. e) Honeycomb lattice, Brillouin zone and 2D electronic dispersion of graphene: (left) electronic structure nearby the Fermi level and (right) zoom in the energy band close to one of Dirac cones. Reproduced with permission.[10] Copyright 2009, American Physical Society.

arrays for radiofrequency transistors achieve a current-gain cutoff frequency of 540 GHz and a power-gain cutoff frequency of 306 GHz.[22] FETs constructed using closely-packed single-walled carbon nanotube (SWNT) arrays on hexagonal boron nitride substrates show mobility up to 2000 $cm^2\ V^{-1}\ s^{-1}$.[23] Magic-angle twisted bilayer graphene (MATBG) devices fabricated via the tear-and-stack dry-transfer technique have enabled the creation of tunable Josephson junctions and single-electron transistors, exhibiting superconducting phase coherence, non-local Josephson effects.[24] Few-layer fullerene nanosheets synthesized via chemical vapor transport and exfoliation have shown remarkable photocatalytic performance for splitting pure water into hydrogen (H_2) and hydrogen peroxide (H_2O_2), potentially useful in energy applications.[25]

The key to unlocking these applications relies on the precise control of electronic properties, which enables the design of high-performance FETs,[21] photodetectors,[26] and sensors[27] based on pure carbons. A representative case is the structural transformation of fullerene, where interconnected C_{60} cages transit from molecular semiconductors to quasi-metallic states via controlled bonding formation between cages.[17] This paradigm shift highlights the critical role of structural hierarchy, where the collective electronic behaviors emerge from the synergistic interactions between nanoscale building blocks. Specifically, the symmetry inheritance across multiple length scales and precisely engineered interface between units serve as the governing principle for transitioning from discrete nanostructures to functional superatomic architectures.

To meet the rapid development in this field, a brief summary of the electronic properties of carbon-based superatomic structures would be timely for the design and application of such carbon materials. This review aims to summarize the research progress on the electronic properties of carbon-based superatomic structures, starting from the electronic properties of traditional carbon crystals to nano carbons. With the focus on those superatomic structures constructed from nano units, the interface between carbon nanostructures and the relationship between hierarchical structure and electronic properties will be highlighted.

2. 3D Atomic Carbon Crystals

Traditional 3D carbon crystals of graphite and diamond demonstrate electronic properties governed by the interaction between carbon atoms, with rich diversity through structural engineering. In graphite (space group $P6_3/mmc$), the sp^2-hybridized covalent bonds construct a planar network, while the van der Waals interlayer interaction forms the stacking structure (Figure 1b), which generates the anisotropy of electronic property: in-plane bonding networks facilitate a high conductivity via delocalized π-electrons,[28] whereas the weak interlayer coupling suppresses out-of-plane charge transport. The stacking order also plays a critical role on the electronic properties of graphite: AB (Bernal) stacking manifests a semi-metallic behavior with Dirac-like band structures near K-points,[29] while ABC (rhombohedral) stacking permits a band gap engineering for semiconductor applications.[30] The electronic properties of graphite give it potential for a wide range of applications in electric devices, energy storage and thermal management.

Diamond, a sp^3-hybridized 3D carbon crystal (space group $Fd3m$), features a tetrahedral covalent network (Figure 1b) that delivers unparalleled mechanical property,[31] including an exceptionally high Young's modulus of approximately 1164 GPa.[32] The wide band gap (≈5.5 eV)[33] renders it electrically insulating, yet defect engineering through boron/phosphorus doping enables a semiconducting property and even superconductivity.[34] Remarkably, such a covalent framework simultaneously supports

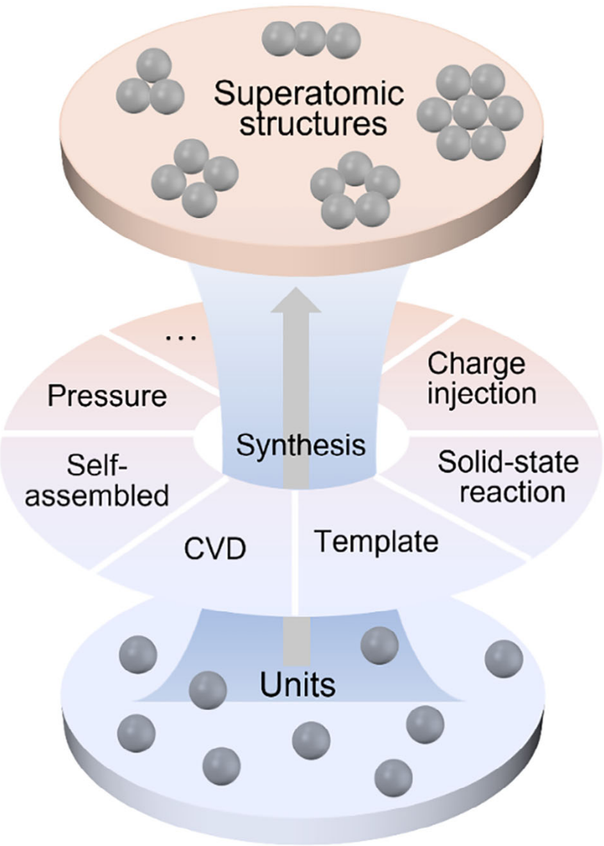

Figure 2. Schematic diagram of synthesis of superatomic structures.

a super-high thermal conductivity (>2000 W m^{-1} K^{-1})[35] and carrier mobility (≈2000 cm^2 V^{-1} s^{-1}),[36] making diamond indispensable for extreme-condition electronics, quantum technology and future semiconductor application. The structural symmetries of graphite and diamond provide a blueprint for designing superatomic materials with analogous functional properties.

3. Carbon Nanostructures

Reducing the dimension to the nanoscale unveils quantum confinement in carbon materials. With dimensionally confined electronic states and emergent quantum effect, carbon nanostructures, such as 0D fullerenes or quantum dots, 1D CNTs and 2D graphene or graphdiyne, have opened the new ear of nanomaterials and nanotechnology by unlocking the potential in optoelectronics,[37] nanoelectronics[38] and so on.

As a representative of 0D carbon nanostructures, fullerene C_{60} has a closed spherical cage comprising 12 pentagons and 20 hexagons.[39] The curvature of the sp^2-hybridized carbon cage in fullerene facilitates delocalized π-electrons and enhances their chemical reactivity.[40] The energy gap of ≈1.64 eV between Highest Occupied Molecular Orbital (HOMO) and Lowest Unoccupied Molecular Orbital (LUMO),[41] and the high electron affinity[42] significantly contribute to the remarkable photochemical and electrochemical activities observed in C_{60}. SAMOs[8] in C_{60} with energy levels ranging from 2.8 to 5.2 eV, as shown in Figure 1c, resemble the s, p, and d orbitals of atoms, enabling atom-like electronic states in C_{60}. Remarkably, SAMOs hybridization can also induce metallic states through the formation of near free electron (NFE) band, making fullerenes potentially usable in nano- and optoelectronics. Johansson et al. experimentally identified SAMOs in gas-phase C_{60}/C_{70} via angle-resolved photoelectron spectroscopy,[43] demonstrating s-SAMOs display characteristic atomic s-orbital symmetry with an anisotropy parameter $\beta \approx 2$ in photoelectron angular distributions, while p/d-SAMOs exhibit higher angular momentum features. Time-dependent DFT calculations verified the electron density localization at the cage center, revealing SAMOs as a universal property of hollow molecular structures. Notably, s-SAMOs show significantly higher ionization efficiency at low photon energies compared to p/d-SAMOs,[44] with ionization timescale (≈10 fs) orders of magnitude faster than valence state ionization, highlighting the dominant role of SAMOs in photoexcitation processes.

CNTs are 1D structures formed by rolling up a graphene sheet, with their electronic states determined by the (n, m) indices, where n and m define the rolling direction based on graphene's lattice basis vectors, as shown in Figure 1d. Armchair-type CNTs (n = m) display a metallically high conductivity (>10^6 S m^{-1}),[45] whereas the zigzag (m = 0) and chiral (n ≠ m) counterparts possess tunable semiconducting bandgaps (0.1–2.0 eV),[46] inversely correlated with tube diameter.[47] Quantum confinement[48] radially restricts the electron motion in SWNTs, enabling a ballistic transport along the axial direction of CNTs with a mobility which can exceed 10^5 cm^2 V^{-1} s^{-1}.[49] Combined with exceptional thermal conductivity (3000–6000 W m^{-1} K^{-1} along the axial direction),[50] CNTs serve as ideal platforms for high-frequency nanoelectronics and quantum sensing.

As the very basic unit of sp^2-hybridized carbon materials, 2D monolayer graphene was prepared from graphite and was soon recognized for its fascinating properties. It features a hexagonal lattice with a linearly dispersed Dirac cone at K point in the Brillouin zone[10] (Figure 1e). Massless Dirac fermions in graphene exhibit ultrahigh carrier mobility (>2×10^5 cm^2 V^{-1} s^{-1} measured at room temperature)[51] and the half-integer quantum Hall effect observed under ambient conditions.[52] Despite the zero bandgap in intrinsic graphene, which has restricted its application in logic devices,[53] the high thermal conductivity (≈5000 W m^{-1} K^{-1}),[54] topological robustness and electric conductivity drive graphene usable in high-frequency electronics, high-end composites and energy storage.

4. Superatomic Structures Formed by Carbon Nanostructures

Due to the essentially infinite possibility of assembly of carbon atoms with various hybridizations, curvatures, and dimensions, carbon-based superatomic structures could have endless candidates, many of which have demonstrated good thermal dynamic stability and feasible preparation route as predicted by theoretical simulations. Readers may refer to some review articles for the structures and general properties of such carbons.[55] Since the current review focuses on the electronic properties of superatomic carbons formed by nanostructures, we will focus on how to integrate the building blocks by a precisely engineered assembling technique and see how the electronic behaviors in different

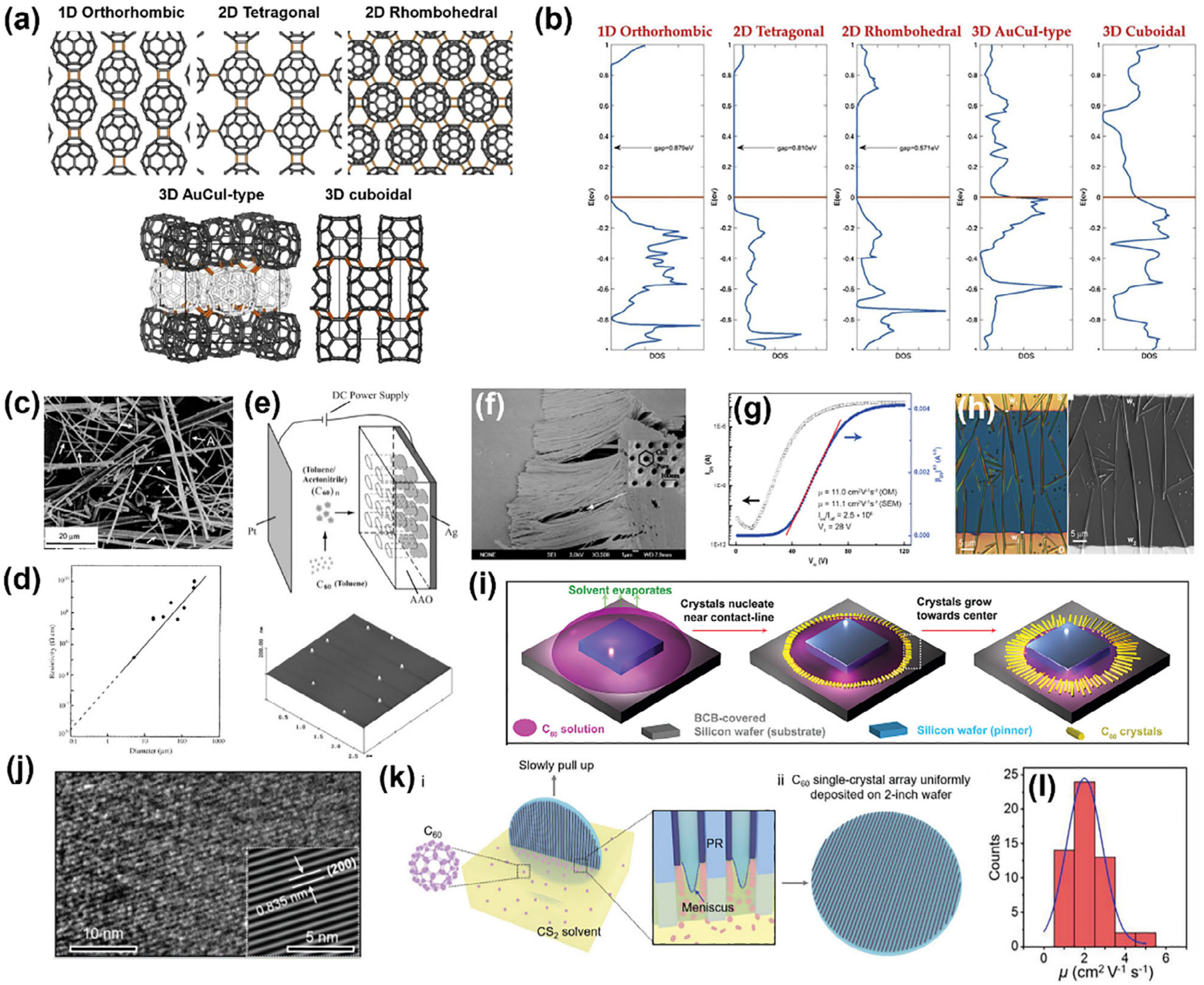

Figure 3. a) Polymerized C_{60} structures and b) corresponding DOS; Reproduced with permission.[17] Copyright 2020, Elsevier. c) scanning electron microscope (SEM) image of C_{60}NWs. Reproduced with permission.[59] Copyright 2003, Wiley-VCH. d) Electrical resistivity of the C_{60} whiskers as a function of diameter. Reproduced with permission.[59] Copyright 2003, Wiley-VCH. e) Schematic illustration of the preparation of C_{60}NW arrays by using anodic aluminum oxide templates (upper); Typical AFM image of C_{60} clusters prepared in acetonitrile/toluene (lower). Reproduced with permission.[60] Copyright 2003, Wiley-VCH. f) Typical SEM image of C_{60}NW array. The inset shows a typical SEM image of the anodic aluminum oxide template. Reproduced with permission.[60] Copyright 2003, Wiley-VCH. g) Transport characteristic of the C_{60}NW device, with mobility (μ), on-to-off current ratios (I_{on}/I_{off}) and threshold voltages (V_T) shown. Reproduced with permission.[21] Copyright 2012, American Chemical Society. h) Left: optical microscopy image of the C_{60}NW device showing one of the needles that bridges the source (S) and drain (D) electrodes. Right: SEM image showing the same needle. Reproduced with permission.[21] Copyright 2012, American Chemical Society. i) Schematic of the droplet-pinned crystallization method.Reproduced with permission.[21] Copyright 2012, American Chemical Society. j) High resolution transmission electron microscope (HRTEM) image of C_{60}NW arrays. Reproduced with permission.[61] Copyright 2021, Wiley-VCH. k) Schematic illustration of the solution-phase epitaxial process for wafer-scale growth of 1D C_{60} single-crystal array. The middle inset shows the confined meniscus within the microscale PR channels. Reproduced with permission.[61] Copyright 2021, Wiley-VCH. l) Mobility statistical histogram of 55 C_{60}NW FETs. Reproduced with permission.[61] Copyright 2021, Wiley-VCH.

nanostructures extend or change in superatomic structures, as illustrated in **Figure 2**.

4.1. Fullerene-Based Superatomic Crystals

4.1.1. Fullerene Polymers

Fullerene polymers, a class of superatomic crystals where C_{60} molecules are interconnected by covalent bonds to form ordered 1D, 2D, or 3D architectures, have garnered significant attention since the 1990s.[56] Early studies on C_{60} crystals, which adopt a face-centered cubic (fcc) structure held together by van der Waals interaction, revealed semiconducting characteristics with a direct band gap of 2.3 eV.[57] Apparently the electronic properties of fullerene-based materials are intricately linked to the structural configuration, which experiences a transition from individual C_{60} molecules to polymeric structures as occurred in conventional polymerization reactions. Generally speaking, increasing the degree of polymerization (e.g., connections with

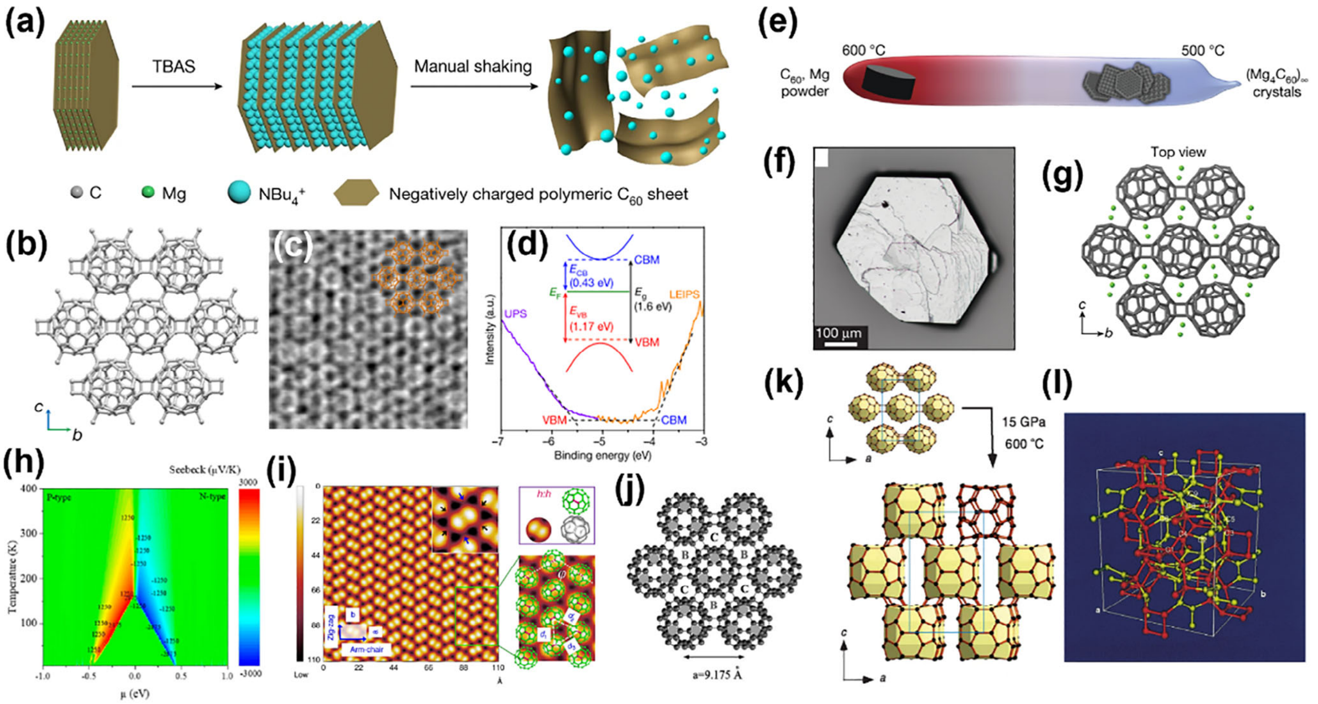

Figure 4. a) Schematic of organic cation slicing exfoliation; Reproduced with permission.[65] Copyright 2022, Springer Nature. b) structure of single crystal qHP C_{60} polymer; Reproduced with permission.[65] Copyright 2022, Springer Nature. c) STEM image of monolayer qHP C_{60} overlaid with geometry structures; Reproduced with permission.[65] Copyright 2022, Springer Nature. d) electronic band structure of the monolayer qHP C_{60} nanosheets measured by the UPS and LEIPS experiments; Reproduced with permission.[65] Copyright 2022, Springer Nature. e) schematic of CVT technique used for $(Mg_4C_{60})_\infty$ preparation. Reproduced with permission.[66] Copyright 2023, Springer Nature. f) Optical micrograph and g) crystal structure of $(Mg_4C_{60})_\infty$. Reproduced with permission.[66] Copyright 2023, Springer Nature. h) Seebeck coefficients of qHP C_{60}; Reproduced with permission. [70] Copyright 2022, American Chemical Society. i) a close-up Scanning Tunneling Microscope (STM) image (I = 30 pA, V_b = 1.05 V) of C_{60} on BP that shows two-lobes of intramolecular contrast. The inset images show six locations of moderately enhanced contrast around each C_{60} molecule.Reproduced with permission.[71] Copyright 2019, Springer Nature. j) Structure model for the rhombohedral C_{60} polymer (left); Top view of a polymerized sheet and (right) side view. Reproduced with permission.[73] Copyright 2003, Elsevier. k) Crystal structure of 3D C_{60} polymer (down) in comparison with the starting 2D C_{60} polymer (top); Reproduced with permission.[74] Copyright 2006, American Physical Society. l) geometry structure of the 3D polymerized C_{60} fullerite. The sp^3 carbon atoms are denoted by the red spheres.Reproduced with permission.[75] Copyright 1999, American Physical Society.

adjacent cages by cycloaddition reaction, as shown in **Figure** 3a) reduces the electronic band gap, shifting the carbon from a semiconductor to a quasi-metallic state, as indicted by the narrowed bandgap and emerging density of states (DOS) at the Fermi level (Figure 3b). Such changes underscore the importance of molecular design and polymerization in tailoring the electronic properties of fullerene polymers,[58] across various dimensions of superatomic structures.

In 1D fullerene crystals, such as C_{60} nanowhiskers or nanowires (C_{60}NWs), the electronic property can be tailored by size and morphology, which can further be controlled by varying the solvent type, concentration, and evaporation rate during the self-assembly synthesis of whiskers/wires. Figure 3c shows single-crystal C_{60}NWs prepared via liquid/liquid interfacial precipitation, in which the C_{60}NWs exhibit a decrease in electrical resistivity with reduced diameter, highlighting the impact of structural integrity on the electron transport (Figure 3d).[59] In contrast, polycrystalline NWs (Figure 3f) were synthesized by a template method (Figure 3e), showing a significantly lower conductivity (6×10^{-6} S m^{-1}).[60] The high electron mobility (11 cm^2 V^{-1} s^{-1}, Figure 3g) observed in single-crystal arrays of NWs (Figure 3h), which are grown by a droplet-pinned crystallization method (Figure 3i), further emphasizes the role of crystallinity in enhancing the electron transport in C_{60}NWs.[21] Similarly, single crystal C_{60}NW arrays (Figure 3j) prepared by solution-phase epitaxial (Figure 3k) exhibit a mobility range of 2.17–5.09 cm^2 V^{-1} s^{-1} (Figure 3l),[61] about one order higher than that of polycrystalline thin films (0.5–0.3 cm^2 V^{-1} s^{-1}).[62] Crystallinity and synthesis methods play a critical role in optimizing the electronic properties of C_{60}NWs for advanced applications.

2D fullerene structures have attracted special interest for electronic devices. Previous research on 2D fullerene polymers has predominantly focused on tetragonal[63] and rhombic[64] phases, which were synthesized through high-pressure and high-temperature polymerization methods. However, the extreme preparation conditions lead to insufficient final yields, limiting the practical utility. To address the challenge of low material yield, an organic cation stripping strategy (**Figure** 4a) has been proposed by Hou et al. to prepare a monolayer quasi-hexagonal phase fullerene network (qHP C_{60}, Figure 4b,c), which demonstrates a semiconducting feature with a band gap of about 1.6 eV (Figure 4d).[65] This structure was also synthesized by Meirzadeh et al. using dilute acid to remove magnesium in magnesium-doped polyfullerene $(Mg_4C_{60})_\infty$ grown with chemical vapor

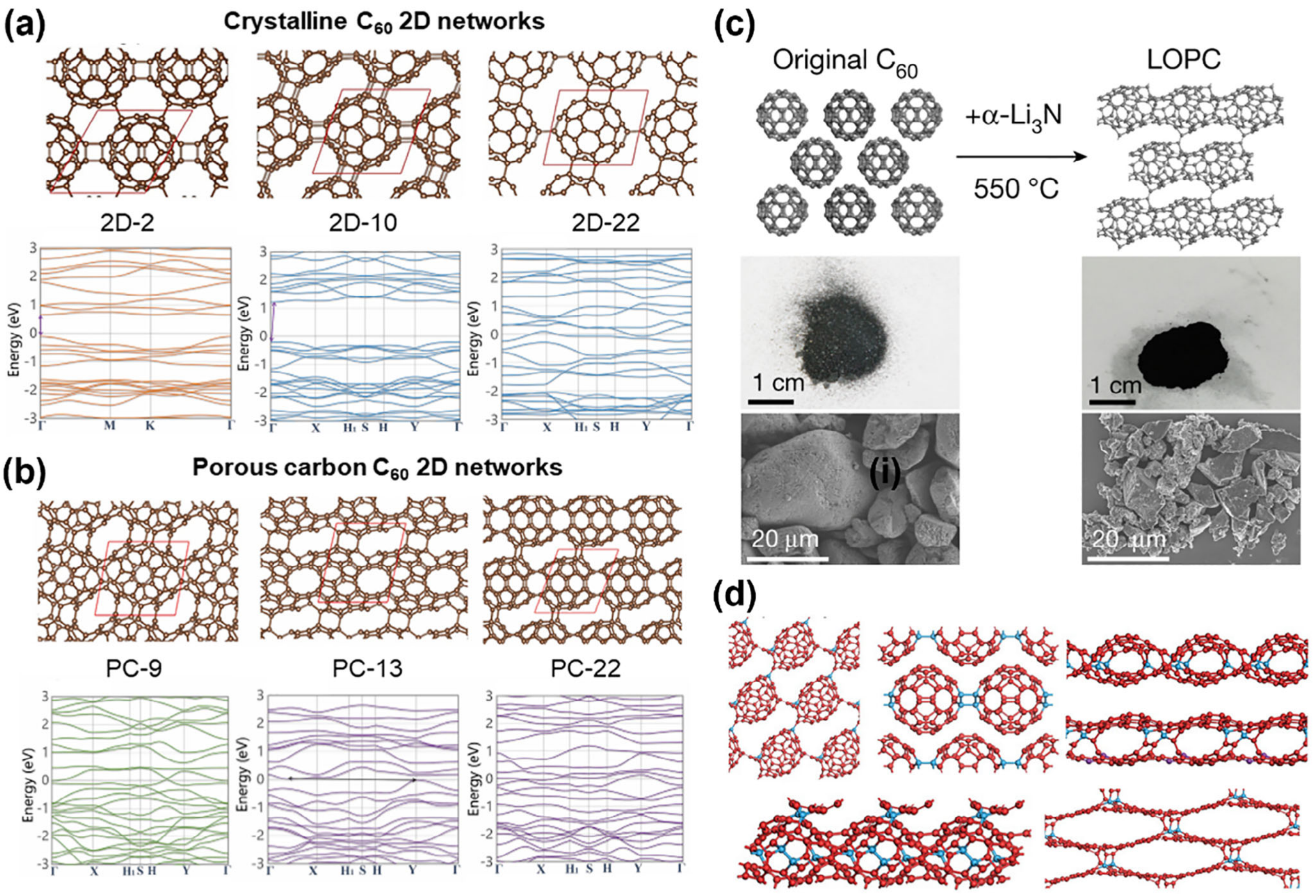

Figure 5. a) Structures of C_{60} based 2D crystalline networks and their corresponding electronic band structures calculated under PBE/GGA level; Reproduced with permission.[76] Copyright 2023, Elsevier. b) structures of produced C_{60} based porous carbon lattice and their corresponding electronic band structures calculated under PBE/GGA level; Reproduced with permission.[76] Copyright 2023, Elsevier. c) atomic structure models, optical and SEM images. Reproduced with permission.[77] Copyright 2023, Springer Nature. d) C_{60} derivative structures; two coordinated carbon atoms are marked as purple; three coordinated carbon atoms are marked as red and four coordinated carbon atoms are marked as blue. Reproduced with permission.[78] Copyright 2022, Wiley-VCH.

transport (Figure 4e–g), followed by mechanical exfoliation.[66] The asymmetric bridging arrangement, where each C_{60} cage is connected to adjacent cages via [2+2] cycloaddition bonds or C-C bonds, endows the network with significant in-plane anisotropy in optical, mechanical, and thermoelectric properties. Following these structural insights, Zhao et al. performed a systematic theoretical study of the electronic structure and chemical bonding for $qHPC_{60}$.[67] The DFT calculations highlighted the critical role of [2+2] cycloaddition and C-C single bonds in stabilizing the structure by facilitating charge redistribution and inducing dual π-aromaticity within C_{60} cages. Moreover, the study identified delocalized SAMOs that hybridize to form NFE bands with σ/π bonding and σ^*/π^* antibonding characteristics. A tight-binding calculation carried out by Xu et al.[68] revealed that the 2D fullerene polymer networks exhibit semiconducting properties but are less stable than individual C_{60} molecules, tending to dissociate at temperatures of 270 °C.[69] Based on the deformation potential theory, Yu et al. revealed that the hole mobility in qHP C_{60} can reach 1242 cm^2 V^{-1} s^{-1}, allowing for thermoelectric applications, especially when coupled with a high Seebeck coefficient at medium and low temperatures (3000 μV K^{-1} at 100 K, Figure 4h).[70] In another work, Cui et al. realized a nearly-free-electron-like conduction band in a C_{60} monolayer (Figure 4i) by mediating intermolecular van der Waals interactions on a black phosphorus (BP) substrate.[71] The BP substrate optimizes the intermolecular π–π overlaps, forming a highly delocalized LUMO band with an effective mass of 0.53–0.70 m_e and carrier mobility of 200–440 cm^2 V^{-1} s^{-1}. Additionally, the electronic properties of the 2D rhombohedral C_{60} superatomic structure are sensitive to the stacking sequence. Using DFT with local-density approximation, Miyake et al. found that the stacking sequence of ABCABC[64] is more stable than ACBACB (Figure 4j),[72] showing different band gaps: 0.68 eV (ABCABC) and 0.58 eV (ACBACB).[73]

3D fullerene crystals can be synthesized from 2D fullerene polymers under high-pressure and high-temperature conditions, often accompanied by a transition of conductivity from semiconducting to metallic type. Yamanaka et al. obtained a 3D fullerene crystal by applying a pressure of 15 GPa to 2D tetragonal C_{60} polymer crystals at 600 °C (Figure 4k), and the resulting crystal exhibits an electrical conductivity of about 10^{-1} to 10^{-2} S cm^{-1} at room temperature.[74] Theoretical studies further predicted that applying a uniaxial pressure to the 2D tetragonal phase C_{60}

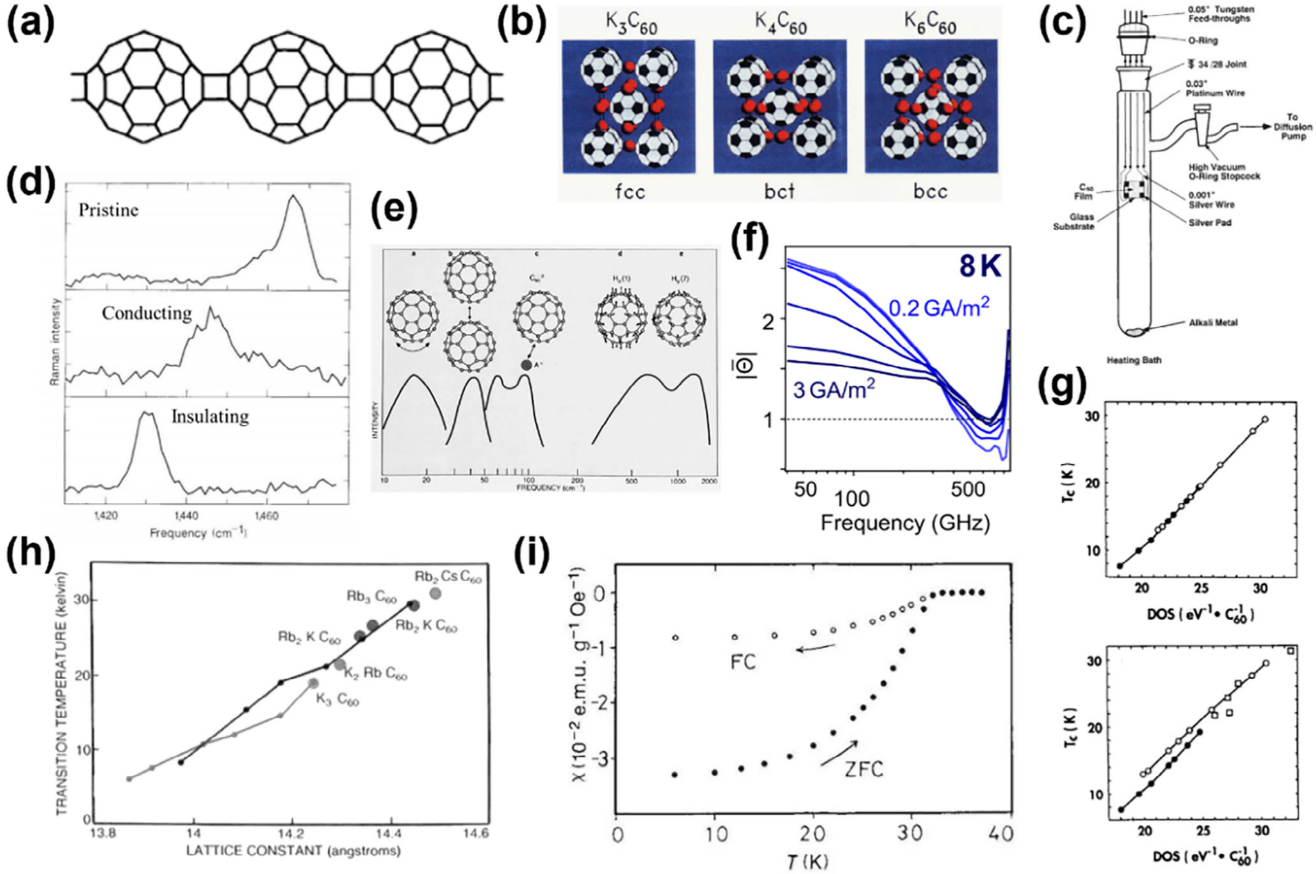

Figure 6. a) Molecular view of [2 + 2] cycloadduct $(C_{60})_n$ polyanion. Reproduced with permission.[84] Copyright 1994, Science. b) Structures of alkali metal doped phases K_xC_{60}: fcc K_3C_{60}, bct K_4C_{60}, and bcc K_6C_{60}; Reproduced with permission.[86] Copyright 1992, American Chemical Society. c) apparatus for vapor-phase doping of C_{60} and C_{70} films. Reproduced with permission.[87] Copyright 1991, Springer Nature. d) In situ Raman spectra of a C_{60} film taken during K doping. Reproduced with permission.[87] Copyright 1991, Springer Nature. e) Various vibrations in A_3C_{60} compounds can contribute to electron-phonon coupling. Reproduced with permission.[83] Copyright 1992, AIP Publishing. f) Current- and frequency-dependent normalized transmittance $|\bar{\Theta}|$ at 8 K. Reproduced with permission.[88] Copyright 2023, Springer Nature. g) Superconducting transition temperature as a function of DOS, obtained by simulation (top) and experiment (down); Reproduced with permission.[89] Copyright 1992, Elsevier. (h) T_c of bulk powder samples of $A_{3-x}A'_xC_{60}$, where A and A' represent K, Rb or Cs, shows a nearly linear dependence on lattice constant. Reproduced with permission.[83] Copyright 1992, AIP Publishing. i) Magnetic susceptibility x as a function of temperature for the sample with nominal composition $Cs_2Rb_1C_{60}$. Reproduced with permission.[90] Copyright 1991, Springer Nature.

could also result in a 3D derivative structure (Figure 4l), with a metallic electronic structure and a high DOS at the Fermi level.[75] In parallel, Mortazavi et al. investigated the electronic properties of C_{60} polymers by the combination of first-principles simulation and machine learning methods.[76] They found that the crystalline C_{60}-based networks (**Figure 5a**) are more likely to exhibit semiconducting properties compared to porous carbon-based fullerene networks (Figure 5b), highlighting the critical role of structural unit connection in determining the electronic behavior of fullerene-derived superatomic structures.

Comprehensive characterizations of fullerene superatomic structures require a higher efficient preparation of such crystals. By highlighting the critical role of electron injection, Pan et al.[77] demonstrated that treating C_{60} with α-Li_3N at a temperature range of 440–600 °C would transform C_{60} molecular crystal into polymerized fullerenes and long-range ordered porous carbon (LOPC) crystals (Figure 5c), which exhibit enhanced electronic delocalization compared to pristine C_{60}. Theoretical simulations suggest that charge injection into C_{60} generates electric dipole moments that propagate along the neighboring molecules, facilitating the formation of covalent bonding between cages. Ni et al.[78] further explored the structural evolution of C_{60} with neural network potential and stochastic surface walking methods and uncovered a large number of superatomic structures from C_{60} (Figure 5d). More DFT calculations showed that the bandgap of these structures is sensitive to the sp^2-hybridized content, providing an insight into the tailoring of electronic properties of such structures. It is worth noting that although the Perdew-Burke-Ernzerhof (PBE) functional has been widely used and computationally efficient, it often underestimates band gaps[79]; more accurate predictions can be achieved using hybrid functional, like the HSE06,[80] or GW method,[81] for the future studies of electronic properties of fullerene polymers.

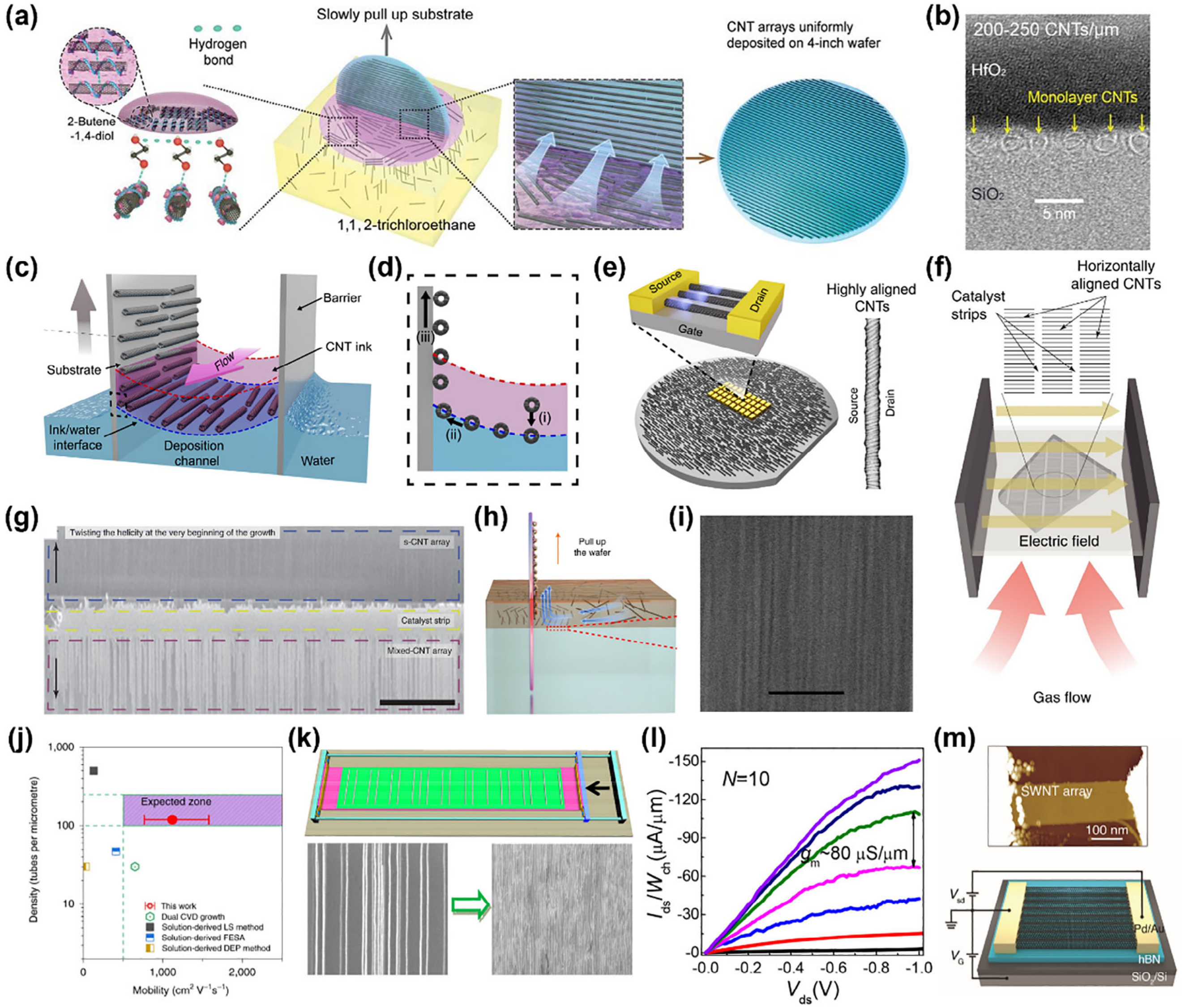

Figure 7. a) Schematic showing the process of preparing a wafer-scale CNT array. Reproduced with permission.[96] Copyright 2020, Science. b) Cross-section TEM image of CNT arrays obtained using a solution concentration of 60 μg/ml, resulting in a density of at least 200 CNTs/mm (<5 nm pitch). Reproduced with permission.[96] Copyright 2020, Science. c) Experimental apparatus for tangential flow interfacial self-assembly. Reproduced with permission.[97] Copyright 2021, Science. d) Magnified view of ink/water interface and alignment process shown in c). Reproduced with permission.[97] Copyright 2021, Science. e) Wafer-scale assemblies of aligned nanotubes; Reproduced with permission.[97] Copyright 2021, Science. f) schematic of the electro-renucleation system; Reproduced with permission. [98] Copyright 2018, Springer Nature. g) SEM image of a bright metallic CNT and a dark semiconducting CNT. Reproduced with permission.[98] Copyright 2018, Springer Nature. h) Schematics illustrating the binary liquid interface-confined self-assembly. Reproduced with permission. [22] Copyright 2021, Springer Nature. i) SEM image showing an as-deposited CNT array on a silicon substrate. Scale bar: 100 nm; Reproduced with permission.[22] Copyright 2021, Springer Nature. j) benchmarking density and carrier mobility of CNTs arrays from shi et al.[22] and other reported CNTs arrays[100]; Reproduced with permission.[22] Copyright 2021, Springer Nature. k) flowchart showing the major steps of the density amplification method; Reproduced with permission.[101] Copyright 2018, American Chemical Society. l) output characteristics of FETs based on high-density CNTs arrays in k). Reproduced with permission.[101] Copyright 2018, American Chemical Society. m) AFM topography and structural schematic of a FETs based on SWNT arrays. Reproduced with permission.[23] Copyright 2025, Science.

4.1.2. Metal Doped Fullerene

One of the most fascinating aspects of fullerene-based superatomic crystals is their ability to exhibit superconductivity upon doping with alkali metals. Since a superconducting transition temperature (T_c) of 18 K was first observed in K_3C_{60} in 1991,[82] researchers have explored the superconductive fullerene by adjusting the types and stoichiometric ratios of doped metals.

Alkali metals (e.g., K, Rb, Cs) and alkaline earth metals (e.g., Ca, Ba) are typical dopants that transfer electrons into the LUMO of C_{6n}, forming intercalation compounds.[83] In alkali metal systems, when the doping concentration is low (e.g., A_1C_{60}, (A = K, Rb, Cs)), the C_{60} molecule forms a 1D polymer chain through a

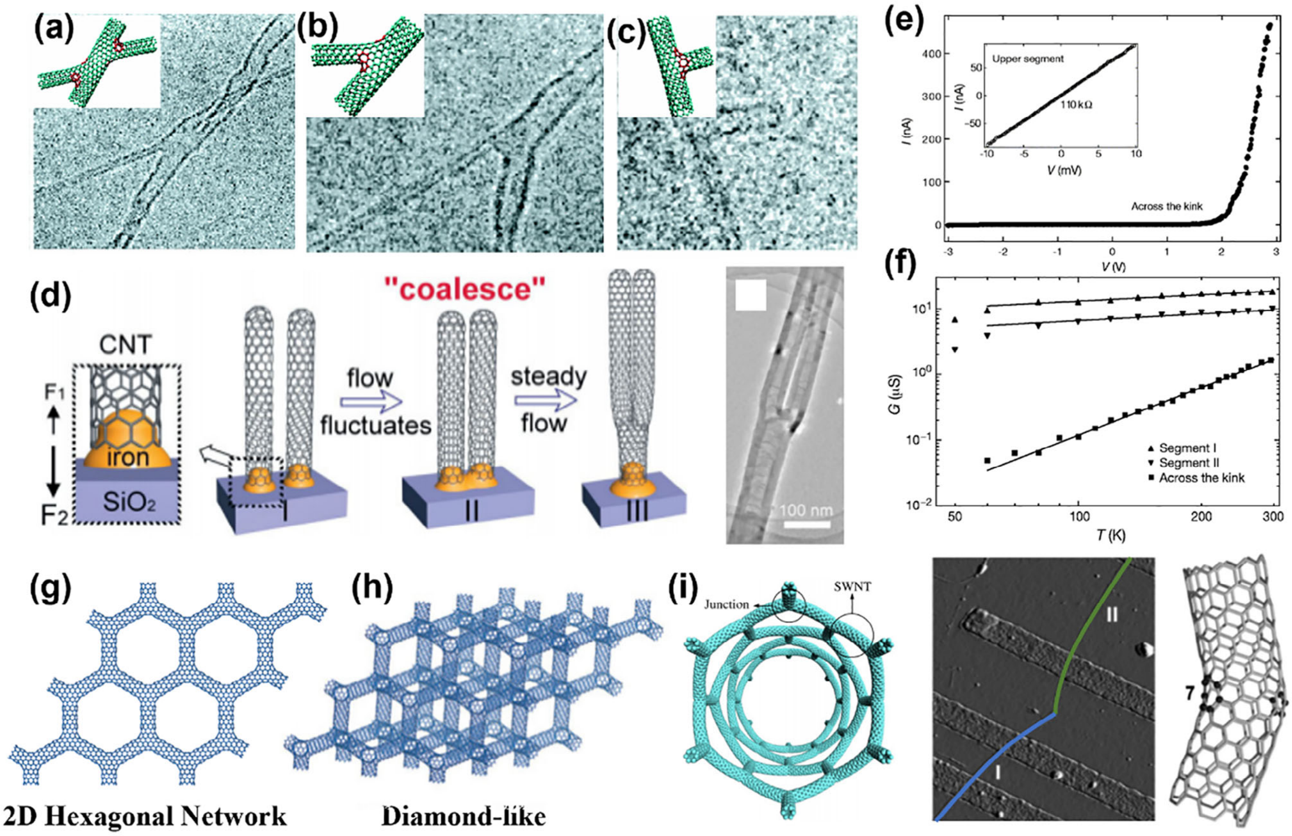

Figure 8. a) HRTEM image of X junction created by 60 s electron beam irradiation; Reproduced with permission.[104] Copyright 2002, American Physical Society. b) HRTEM image of Y junction created by removing one of the arms of X junction with electron irradiation; Reproduced with permission.[104] Copyright 2002, American Physical Society. c) HRTEM image of T junction by irradiating Y junction. Insets in a,b, and c) show the geometry model of each junction, with heptagonal rings marked in red; Reproduced with permission.[104] Copyright 2002, American Physical Society. d) schematic of the formation process of branched nanostructures (left) and a branched CNT produced on a SiO_2 substrate (right). Reproduced with permission.[105] Copyright 2007, Wiley-VCH. e) Current–voltage curve measured across the metal-semiconductor junction, showing a rectifying behavior; Reproduced with permission.[106] Copyright 1999, Springer Nature. f) linear response of two-probe conductance of segments I and II shown in i), across the metal-metal junction. The data are fitted by the scaling power law $G(T) \propto T^{\alpha}$, associated with the suppression of tunneling density of states in a Luttinger liquid (top); The tapping-mode AFM amplitude images of metal-metal CNTs junction device with green and blue lines representing two different metal nanotubes (down, left); Illustration of the carbon network of a kink junction constructed between an "armchair" tube and a "zigzag" tube, where 5 denotes a pentagon, 7 denotes a heptagon (down, right). Reproduced with permission.[106] Copyright 1999, Springer Nature. g) Structure model of 2D hexagonal SWNT network; Reproduced with permission.[109] Copyright 2011, American Chemical Society. h) structure model of 3D diamond-like SWNT architectures; Reproduced with permission.[109] Copyright 2011, American Chemical Society. i) structure model of [6, 0]@(6, 0) SWNT superstructures. Reproduced with permission.[110] Copyright 2006, IOP Publishing.

[2+2] cycloaddition reaction[84] (**Figure 6a**). As the doping level increases to A_3C_{60}, the system tends to adopt an fcc structure, with metal ions occupying the octahedral and tetrahedral interstitial sites while the C_{60} molecule remains rotationally disordered. Under saturated doping conditions (e.g., K_6C_{6n}), the molecular arrangement of C_{60} is transformed into a body-centered cubic (bcc) structure (Figure 6b), and the system exhibits properties of a Mott insulator.[85]

Haddon et al. synthesized alkali-metal-doped C_{60} and C_{70} films deposited on glass substrates using vapor-phase doping (Figure 6c).[87] As the doping progresses, the color of C_{6n} films changes from yellow to metallic gray, and their resistivity decreases dramatically, with the highest conductivity of 500 S cm^{-1} for K-doped C_{60}. Raman spectroscopy reveals that the frequency of the A_g vibrational mode shifts to lower values with increased doping, indicating the electron transfer from metal to C_{6n} (Figure 6d). Rb_3C_{6n} exhibited a superconducting T_c of 28 K.[91] The emergence of superconductivity has been attributed to electron-phonon coupling, where molecular vibrations (phonons) (Figure 6e) play a crucial role in mediating the pairing interaction.[83, 86]

Wang et al. fabricated K_3C_{60} thin films using molecular beam epitaxy, displaying distinct nonlinear current-voltage characteristics (Figure 6f), which are indicative of photo-induced granular superconductivity.[88] K doping is considered to significantly alter the electronic structure of C_{60}, leading to redistributed electrons and enhanced electron interactions, thereby promoting superconductivity in a non-equilibrium state. Oshiyama et al. observed that the incorporation of K/Rb transforms C_{60} into a strongly bonded ionic metal, explaining the linear dependence of superconducting T_c on the DOS near the Fermi level,[89] shown in Figure 6g. Doping also changes the lattice structure: as the

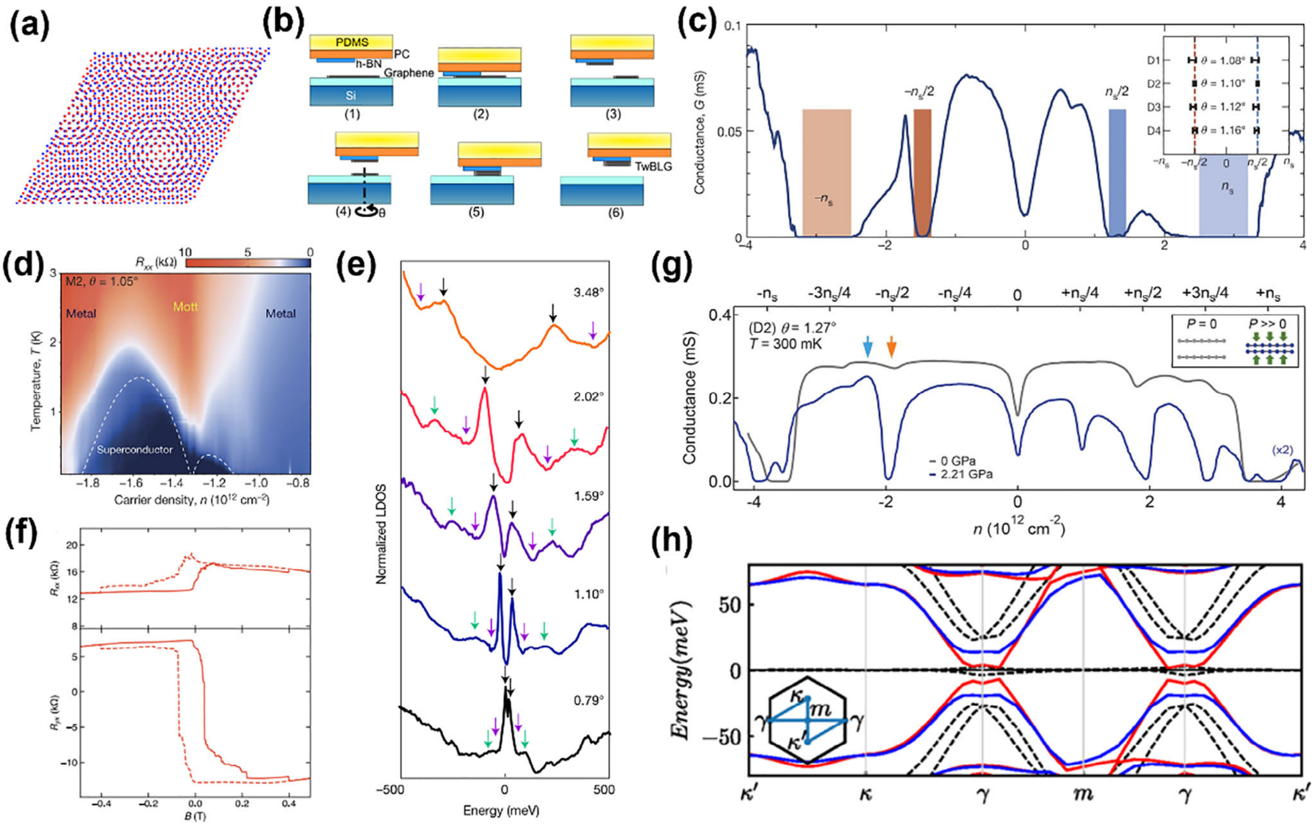

Figure 9. a) Structure of moiré supercell of the tBLG; Reproduced with permission.[114] Copyright 2023, Wiley-VCH. b) illustration of "Tear & Stack" technique. Reproduced with permission. [115] Copyright 2016, American Physical Society. c) Half-filling insulating states in MATBG, showing measured conductance G for device D1 with $\theta = 1.08°$ and $T = 0.3$ K. Inset: half-filling states in four devices; Reproduced with permission.[116] Copyright 2018, Springer Nature. d) four-probe resistance R_{xx} versus temperature. The device exhibits two asymmetric and overlapping domes with the highest critical temperature of $T_c = 1.7$ K; Reproduced with permission.[15] Copyright 2018, Springer Nature. e) SPS measured local DOS at zero electron doping on moiré AA sites with twisting angle of 3.48, 2.02, 1.59, 1.10, and 0.79°. The van Hove singularities (black arrows), first dips (purple arrows), and a second smaller peak (green arrows) are shifting toward the Fermi level as the twist angle decreases;Reproduced with permission.[117] Copyright 2019, Springer Nature. f) magnetic field dependence of the longitudinal resistance R_{xx} (upper) and Hall resistance R_{yx} (lower); Reproduced with permission.[118] Copyright 2019, Science. g) conductance of device D2 (1.27°) at 0 GPa (gray) and 2.21 GPa (blue) at $T = 300$ mK. Inset: schematic illustration of reduced interlayer spacing in tBLG under pressure; Reproduced with permission.[119] Copyright 2019, Science. h) energy dispersion of C_2T breaking (blue) and C_2T preserving (red) states at $\theta = 1.1°$ and effective dielectric constant (ε) = 5. Dotted lines show noninteracting flat bands. The inset shows high-symmetry lines in the moiré Brillouin Zone. Reproduced with permission.[120] Copyright 2020, American Physical Society.

intercalated ions increase the lattice constant expands, which in turn increases the DOS at the Fermi level and enhances T_c (Figure 6h).[87, 92] Notably, hybrid doping can optimize the lattice parameters by adjusting ion size matching. For example, $Cs_2Rb_1C_{60}$ shows a superconducting phase with T_c up to 33 K at a lattice constant of a = 14.65 Å[90] (Figure 6i).

However, doping with alkaline earth metals results in distinct structural arrangements compared to alkali metal doping. For example, Ca_5C_{60} achieves a superconducting transition ($T_c = 8.4$ K) in a simple cubic structure.[93] In contrast, the body-centered cubic phase of Ba_6C_{60} (a = 11.17 Å), despite having a similar electron filling, exhibits a low T_c of 7 K due to the small molecular spacing (≈9.67 Å).[94] The exploration of doped fullerene highlighted the critical role of metal doping and lattice engineering in optimizing superconducting properties of such superatomic carbons, providing valuable insights for the design of new superconducting materials based on fullerene.

4.2. CNT-based Superatomic Structures

4.2.1. Van der Waals Stacked Carbon Nanotubes

The van der Waals assembly of CNTs may optimize their collective electronic properties. High-purity semiconductor CNTs are essential for advancing high-performance electronic devices. Since impurities significantly degrade charge transport, achieving high purity preparation of CNTs is of vital importance. Researchers have achieved large-scale synthesis of high-purity semiconductor CNT arrays through various innovative strategies, such as CVD, template-guided growth and self-assembly techniques.[95] Liu et al. developed a dimension-limited self-alignment process (**Figure 7a**), enabling the fabrication of semiconductor arrays with a purity exceeding 99.9999% and a density of 200 CNTs μm^{-1},[96] as shown in Figure 7b. Similarly, Jinkins et al. utilized self-organized liquid crystal to form a nematic phase order at the liquid/liquid interface (Figure 7c,d), achieving a

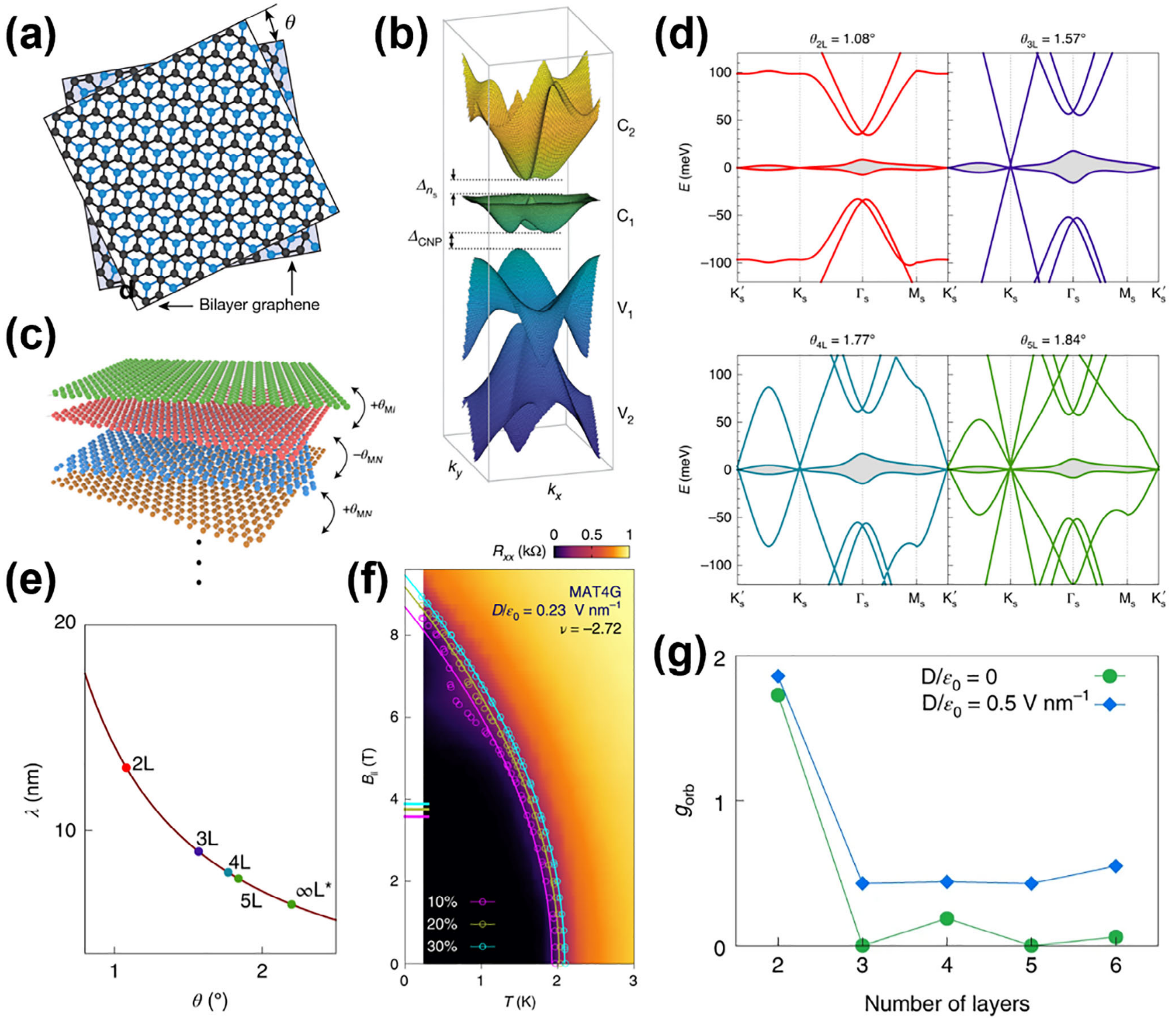

Figure 10. a) Schematic of TDBG with twist angle θ. Reproduced with permission.[125] Copyright 2020, Springer Nature. b) Calculated band structure for $\theta = 1.33°$ TDBG at an optimal displacement field. k_x and k_y are wave vectors in x and y directions. Reproduced with permission.[125] Copyright 2020, Springer Nature. c) Twisted multilayer graphene with alternating twist angles θ_{MN} and $-\theta_{MN}$ between the adjacent layers. Reproduced with permission.[126] Copyright 2022, Springer Nature. d) Single-particle band structures for TBG (red), TTG (blue), T4G (cyan), and T5G (green). e) Dependence of the moiré wavelength λ on the twist angle. Reproduced with permission.[126] Copyright 2022, Springer Nature. f) $B_{||}$-T phase diagram at $(\nu, D/\varepsilon_0) = (-2.72, 0.23\ \mathrm{V\,nm^{-1}})$. Reproduced with permission.[126] Copyright 2022, Springer Nature. g) Calculated orbital g-factor, g_{orb}, for N-layer magic-angle twisted multilayer graphene. Reproduced with permission.[126] Copyright 2022, Springer Nature.

uniform wafer-level deposition (Figure 7e).[97] The solution-based methods complement the electro-renucleation (Figure 7f),[98] which produces high-purity semiconductor tubes (Figure 7g) through the regulation by an electric field. Furthermore, precise synthesis calls for the chiral engineering of the CNTs. Yang et al. utilized W_6Co_7 nanocatalysts as the structural template to achieve direct growth of (14,4) tubes with a purity of ≈97%.[99] Despite the progress above, the presence of metallic tube residues in traditional CVD growth needs to be further stressed.

Breakthrough in optimizing the electrical performance of CNTs has shifted from fundamental research to device applications. The precise alignment and arrangement of CNTs have been a critical factor for improving the charge transport efficiency.[102] For instance, Shi et al. fabricated a CNT array (Figure 7i) with a density of approximately 120 CNTs μm^{-1} and achieved a carrier mobility of up to 1580 cm^2 V^{-1} s^{-1} (Figure 7j), using a double-dispersion sorting and binary liquid interface-confined self-assembly process (Figure 7h),[22] based on which the radiofrequency transistors exhibit a high power gain of 23.2

dB. Si et al. increased the density of CNTs array by 10-fold while maintaining the alignment through a directional shrinking transfer method (Figure 7k),[101] where a high carrier mobility of 1600 $cm^2\ V^{-1}\ s^{-1}$ was obtained and the FETs based on the high-density arrays achieve a record on-state current density of 150 $\mu A\ \mu m^{-1}$ (Figure 7l), significantly advancing FETs based on CVD grown CNTs.[103] Recently, Zhang et al. achieved the growth of closely-packed SWNT arrays on hexagonal boron nitride substrates (Figure 7m), which were used to construct FETs with mobility of 2000 $cm^2\ V^{-1}\ s^{-1}$, an on/off ratio of $\approx 10^7$, and a maximum current density of $\approx 6\ mA\ \mu m^{-1}$.[23] The alignment of CNTs enhances their electronic properties by reducing interfacial defects and minimizing electron scattering, thereby enhancing carrier mobility. Moreover, the high CNT density increases the current-carrying capacity, which is essential for attaining both high driving currents and superior transconductance in FETs. These findings underscore the critical role of integrating precise alignment, advanced transfer and innovative growth strategies for optimizing the electronic properties of van der Waals stacked CNTs for high-performance electronic devices.

4.2.2. Covalently Bonded Carbon Nanotubes

Covalent connection of CNTs offers new possibilities for designing high-performance nano devices. X, Y, and T shaped junction connections between SWNTs have been achieved experimentally by electron beam welding method, as shown in **Figure** 8a–c.[104] The formation of vacancy defects during the electron beam radiation promotes the carbon atom rearrangement by activating dangling bonds, facilitating cross-linking between nanotubes, and driving the formation of non-hexagonal rings. Wei et al. successfully synthesized branched CNTs by introducing flow fluctuation into the vapor-liquid-solid process (Figure 8d).[105] Flow fluctuation causes the catalyst particles to coalesce, which can be tuned to the positions and numbers of these branches. Yao et al. experimentally measured the electronic properties of metal-semiconductor and metal-metal junctions in SWNTs.[106] A rectifying behavior has been determined from the metal-semiconductor junction (Figure 8e), while the metal-to-metal junction exhibits a strong conductance suppression, consistent with the tunneling behavior of the Luttinger liquid model[107] (Figure 8f). Beyond these findings, multi-terminal molecular junctions, such as X/Y/T junctions, offer promising potential for logic gate applications through chiral manipulation.[108] Nevertheless, a key challenge lies in the abrupt drop in conductivity at junction nodes, particularly in hybrid chiral networks with semiconducting SWNTs.[55] To address this challenge, it is crucial to achieve atomic-level structural design when concurrently optimizing the macroscopic structure of the CNT networks.

Theoretical studies have revealed the unique electronic properties of SWNT junctions, including common types such as Y-junctions, T-junctions, X-junctions and multi-terminal junctions, exhibiting distinct electronic behaviors and potential applications in nanoelectronics and quantum devices. In Y-junctions, when the C_3 axis is centered on a six-membered ring, the central region exhibits local C_6 symmetry. This symmetry stabilizes the central region of the Y-junction and opens a band gap.[111] Further research indicates that the rectifying behavior in Y-junctions arises from the interface between semiconducting and metallic electrodes, rather than the intrinsic properties of the junction itself.[112] When semiconducting nanotubes are coupled to metallic leads, interfacial states emerge, acting as scattering centers that impede the electron transmission, resulting in asymmetric conductance curves and rectifying behavior. In the case of T-junctions, defect states cause the Fermi pinning effect, enabling electron transport through quantum tunneling.[113] In configurations such as (5, 5)-(10, 0)-(5, 5) and (9, 0)-(10, 0)-(9, 0) junctions, the presence of heptagonal and pentagonal rings introduces localized electron states within the original band gap region. These localized states serve as tunneling pathways, enabling efficient electron transport across the junction. The theoretical insights into the electronic behavior of SWNT junctions demonstrate the potential of covalent connection structures for the advanced design of nano-devices.

Beyond single junctions, SWNTs can be interconnected to form more complex networks, creating superstructures that exhibit high conductivity and mechanical stability.[109] This approach significantly expands the design possibilities for nanocircuits using SWNTs as fundamental building blocks. The electronic properties of SWNT superstructures have been studied using ab initio calculations. Zhou et al.[109] proposed several stable semiconducting 2D hexagonal (Figure 8g) and metallic 3D diamond-like SWNT superstructures with topological defects (Figure 8h). With more delicate design, SWNT superstructures formed by chiral Y-junctions (Figure 8i) exhibit remarkable stability. With some structures (e.g., [4, 0]@(8, 0)) being even more stable than C_{60},[110] studies show that DOS of these SWNT superstructures is influenced by the structural feature of constituent SWNTs, displaying metallic or semiconducting properties. The presence of Y-junctions and the reduced symmetry in the superstructure led to a smaller bandgap than that of the constituent SWNTs.

4.3. Graphene-Based Superatomic Structures

4.3.1. Magic-Angle Twisted Graphene

MATBG, a 2D material with unique electronic properties, has attracted extensive attention in recent years. Twisted bilayer graphene (tBLG) can be regarded as a superlattice composed of monolayer graphene, assembled by van der Waals interaction, as shown in **Figure** 9a. Each graphene layer in tBLG carries π frontier orbitals, providing possibilities for the design of an electron correlation system through the modulation of interlayer coupling.[114] The collective quantum states from discrete structural units of graphene meet the core paradigm of "artificial atoms" in superatomic crystals. In early research tBLG was successfully fabricated using mechanical exfoliation and stacking techniques.[115] Cao et al.[116] further developed a modified "tear and stack" technique (Figure 9b) and achieved a precise control of the twisting angle (θ) near the magic angle (approximately 1.1°) with an accuracy of 0.1 to 0.2°, enabling to explore a variety of novel physical phenomena in MATBG.

MATBG exhibits a flat band near the charge neutrality point,[121] giving rise to a series of interesting physical

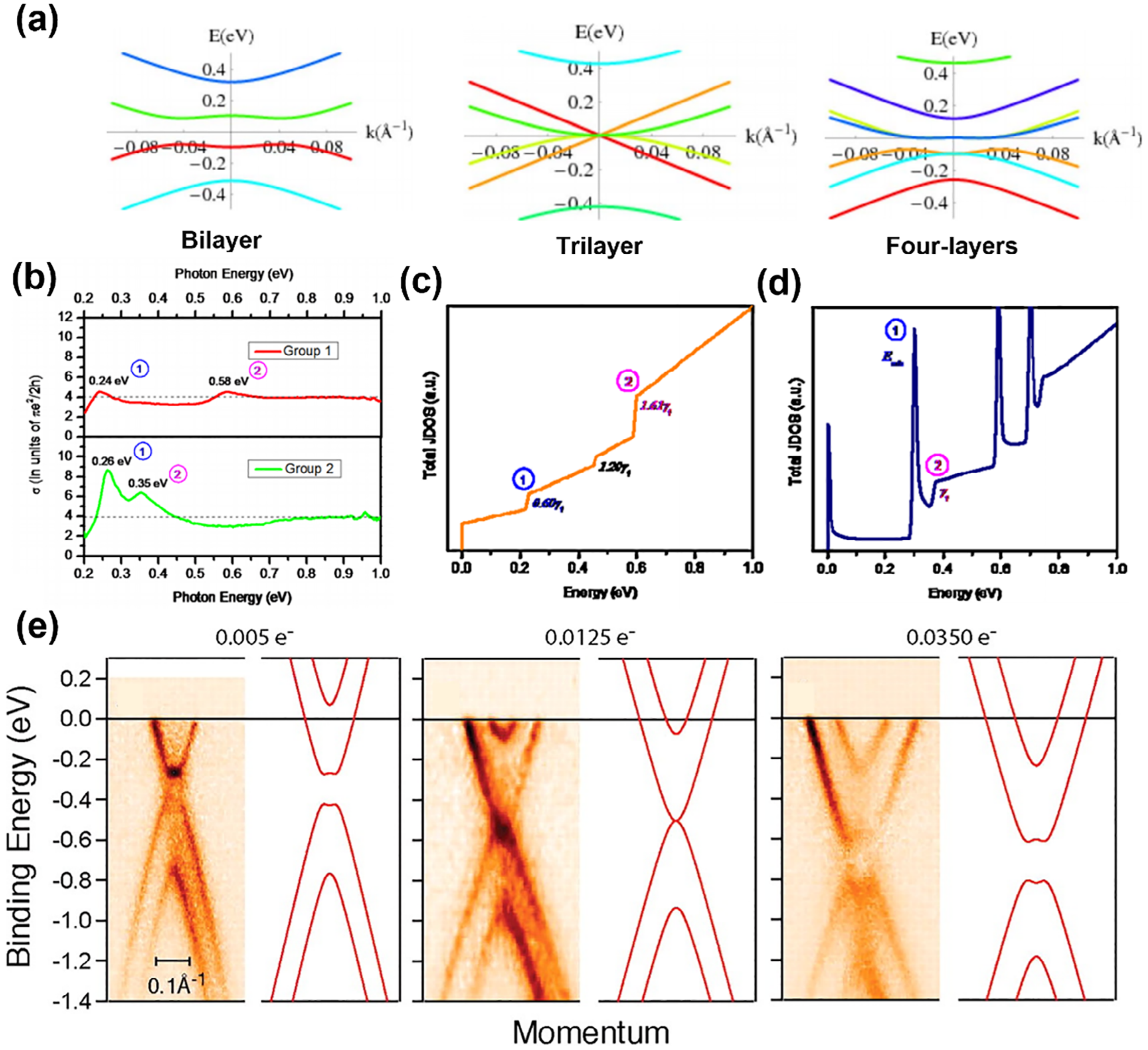

Figure 11. a) Electronic bands of bilayer, trilayer and four-layer graphene; Reproduced with permission.[10] Copyright 2009, American Physical Society. b) infrared optical conductivity spectra $\sigma(\hbar\omega)$ of four-layer graphene in different stacking orders, group 1 represents AB-stacking and group 2 represents ABC-stacking; Reproduced with permission.[18] Copyright 2010, American Physical Society. c) total joint DOS for allowed transitions within the experimentally relevant range of energy in AB-stacked graphene and d) ABC-stacked graphene; Reproduced with permission.[18] Copyright 2010, American Physical Society. e) evolution of gap opening, closing and re-opening by changing the doping level with K deposition.Reproduced with permission.[130] Copyright 2006, Science.

phenomena. Cao et al. observed the correlated insulating states at half-filling for a twisting angle of 1.08° (Figure 9c)[116] and superconductivity with a critical temperature of up to 1.7 K at 1.05° (Figure 9d)[15] in MATBG. Kerelsky et al.[117] observed two distinct van Hove singularities in the local DOS near the magic angle using STM and scanning tunneling spectroscopy (SPS). The energy separation between these van Hove singularities decreases as the twisting angle is reduced, reaching a minimum of 7 to 13 meV at an angle of 0.79° (Figure 9e). HRTEM revealed a cascade of electronic transitions driven by Coulomb interaction, splitting the flat band into Hubbard sub-bands.[122] Moreover, MATBG exhibits ferromagnetism at three-quarters filling, accompanied by giant anomalous Hall effect of 10.4 kΩ (Figure 9f) and signs of chiral edge states, suggesting the emergence of a Chern insulating state.[118] These phenomena arise from enhanced electronic interactions within the flat bands of the MATBG superatomic structures. External pressure and electric fields can further manipulate the electronic properties of MATBG. Yankowitz et al.[119] modulated the interlayer spacing of MATBG with hydrostatic pressure and successfully induced superconductivity at 1.27°

Table 1. Types of fullerene based superatomic structures, synthesis or simulation methods, key electronic property changes, and references.

Superatomic structure		Synthesis/Simulation approach	Key electronic property changes	Refs.
Fullerene polymer	C_{60} nanowhiskers	Liquid/liquid interfacial precipitation method	Electrical resistivity decreases with diameter	[59]
	Polycrystalline C_{60} nanowires	Electrodeposition using anodic aluminum oxide templates	Semiconducting behavior; conductivity ≈6×10^{-6} S m^{-1}	[60]
	Aligned C_{60} single-crystal needles and ribbons	Solution processing method (droplet-pinned crystallization)	Electron mobility up to 11 cm^2 $V^{-1}s^{-1}$ (average: 5.2 ± 2.1 cm^2 $V^{-1}s^{-1}$ for needles, 3.0 ± 0.87 cm^2 $V^{-1}s^{-1}$ for ribbons)	[21]
	Aligned C_{60} single-crystal array	Solution-phase epitaxial growth using microchannel templates	Electron mobility up to 5.09 cm^2 $V^{-1}s^{-1}$ (average: 2.17 cm^2 $V^{-1}s^{-1}$)	[61]
	Polycrystalline C_{60} thin-films	Molecular beam deposition	Field-effect mobility up to 0.56 cm^2 $V^{-1}s^{-1}$	[62]
Metal doped fullerene	K_3C_{60} thin films	Molecular beam epitaxy	Photo-induced granular superconductivity; nonlinear current-voltage responses	[88]
	$(KC_{60})_n$ linear polymer	Co-evaporation method	Metallic conductivity	[84]
	RbC_{6n} and KC_{6n} polymeric chains	Solid-state reaction	One-dimensional metallic behavior	[84]
	alkali-doped C_{6n}		Transformation from semiconductor to ionic metal; increased density of states at Fermi level	[89]
	$Cs_xRb_yC_{60}$		Highest T_c (33 K) and large diamagnetic shielding	[90]
	Ca_5C_{6n}		Superconductivity T_c at 8.4 K	[93]
	Ba_6C_{6n}		Superconductivity T_c at 7 K	[94]

(Figure 9g). Stepanov et al.[123] introduced a metallic graphite screening layer and adjusted its distance from the MATBG. It was found that when the screening layer is closer than 15 nm to the MATBG and the twisting angle is slightly deviated by 1.10 ± 0.05°, the correlated insulating states are quenched, and superconducting states emerge in their place. Clearly, the development of experimental techniques has provided a great foundation for exploring the rich physics in MATBG.

Theoretical studies have further extended the understanding of the electronic properties of MATBG under extreme conditions. Ge et al.[124] demonstrated that large-angle twisted bilayer graphene under pressure can also exhibit flat bands and van Hove singularities near the Fermi level, offering new opportunities to explore the correlated electronic phenomena for twisting angles larger than the conventional magic angle. Xie et al.[120] used the self-consistent Hartree-Fock method to analyze the properties of insulating states in MATBG and found an opened gap due to spin-valley symmetry breaking (Figure 9h), enabling insulating states at $n = \pm p/4$. Interestingly, these states can form without breaking C_2T symmetry, which may prevent a quantized anomalous Hall effect.

In twisted double bilayer graphene (TDBG), the twist angle and stacking configuration play crucial roles in modulating electronic properties. By rotating two sheets of Bernal-stacked BLG to a specific angle (e.g., ≈1.33°), TDBG forms a moiré superlattice structure (**Figure** 10a), generating flat bands with a narrow bandwidth (Figure 10b), caused by significantly enhanced electron correlation.[125] Additionally, the stacking induces spin-polarized states, particularly at half-filling, where electron spins spontaneously polarize, exhibiting ferromagnetic behavior. While TDBG demonstrates strong correlation effects, more complex phenomena emerge in multilayer systems. Park et al. investigated the structure and electronic properties of the magic-angle twisted multilayer graphene (Figure 10c) family.[126] They revealed that stacking graphene layers at specific magic angles leads to the formation of flat bands with minimal dispersion (Figure 10d), which are crucial for the emergence of superconductivity. As the number of layers increases, the magic angle grows while the moiré length scale decreases (Figure 10e), leading to significant modifications in the electronic structure, particularly for $N \geq 3$ systems where additional Dirac cones emerge and coexist with the flat bands. These structural changes substantially enhance superconductivity, enabling it to withstand high parallel magnetic fields far above the conventional Pauli limit (Figure 10f). Figure 10g shows the orbital g-factor (g_{orb}) significantly decreases as the number of layers increases for different layer numbers ($N = 2, 3, 4, 5$, and 6) in the magic angle structure. These findings suggest that precise control of the number of layers and stacking configurations can tune the electronic properties of graphene stacking, making it possible to develop new superatomic carbons with specific functions.

4.3.2. Multilayer Graphene Stacked Structure

More generally, precise control over stacking order and layer numbers in multilayer graphene would enable more tailorable modification of electronic properties, offering more possibilities for electronic devices based on graphene superatomic structures. Theoretical investigations using tight-binding methods have demonstrated that the AB-stacked graphene superatomic structure exhibits Dirac cone characteristics, while the ABC-stacked graphene displays distinct dispersion relations.[10] This fundamental distinction arises from the different symmetry:

Table 2. Types of CNT based superatomic structures, synthesis or simulation methods, key electronic property changes, and references.

Superatomic structure		Synthesis/Simulation approach	Key electronic property changes	Refs.
Van der Waals Stacked CNTs	CNT arrays	dimension-limited self-alignment	Higher on-state current (1.3 mA μm^{-1}), transconductance (0.9 mS/μm)	[96]
		Electro-renucleation approach	High semiconducting purity (<0.1% metallic CNTs)	[98]
		Double-dispersion sorting and binary liquid interface-confined self-assembly	High carrier mobility (up to 1580 cm^2 V^{-1}s^{-1}), high on-state current (1.92 mA μm^{-1})	[22]
		Directional shrinking transfer method combined with thermocapillary flow purification	High on-state current (150 μA μm^{-1}), transconductance (80 μS μm^{-1}), and high on/off ratio (>10^4)	[101]
	(14,4) CNT arrays	Water-assisted CVD growth using W_6Co_7 nanocatalysts	High semiconducting purity (99.8%), Experimental band gap (0.95 eV)	[99]
	Homochiral CNT van der Waals crystals	CVD growth on hBN substrates	High carrier mobility (up to 2000 cm^2/Vs), high on/off ratio ($\approx$10^7), and high current density ($\approx$6 mA/μm)	[23]
Covalently bonded CNTs	Intramolecular junctions in SWNTs	Screened pentagonal-heptagon defective CNTs	Rectifying diode behavior in metal-semiconductor junctions; tunneling in metal-metal junctions	[106]
	Y-junctions in SWNTs	Tight-binding molecular dynamics simulations	Non-conduction energy window in certain symmetries	[111]
	T-junctions in SWNTs	Generalized tight-binding molecular dynamics	Defect-induced localized states	[113]
	2D and 3D SWNT superarchitectures	Covalent assembly of SWNTs with Y- and T-junctions	Semiconducting (2D) or metallic (3D) behavior; high density of states near Fermi level	[109]
	Super-carbon nanotubes	Rolling super-graphene sheets into seamless cylinders	Metallic or semiconducting behavior depending on SWNTs and junctions	[110]

while AB stacking maintains both A/B sublattice symmetry and spatial inversion symmetry – with interlayer coupling mediated by nonlocal orbital hybridization that preserves linear dispersion near the K point, ABC stacking adopts a helical symmetry that breaks inversion symmetry, thereby enhancing the effective interlayer coupling. These symmetry-mediated effects become particularly pronounced in multilayer graphene. Avetisyan et al.[127] demonstrated that ABC-stacked trilayer graphene develops a substantially larger band gap compared to ABA-stacked trilayers, which is a direct manifestation of the stronger interlayer coupling that increases electron localization and dramatically reconstructs the electronic bands. The stacking dependence persists in thicker systems, with four-layer graphene showing significantly larger band gaps in non-Bernal stacking configurations compared to conventional Bernal stacking.

As the layer number increases, stacked graphene progressively manifests the enhanced metallic characteristic (**Figure** 11a) due to substantially increased electronic DOS near the Fermi level.[10] Notably, Dirac fermions emerge exclusively in odd-numbered-layer graphene,[128] arising from the fact that the interlayer coupling in odd layers fails to fully disrupt the sublattice symmetry. The AB stacking of even layers exhibits stronger interlayer coupling compared to odd layers, resulting in the parabolic Dirac cone, highlighting the unique electronic properties driven by layer parity and stacking-dependent symmetries. Studies on low-energy electronic structures of multilayer graphene further reveal chiral decomposition characteristics and Landau level behaviors, with the pseudospin chirality sum always equal to the layer number N.[129]

Experimental characterizations with Raman spectroscopy and infrared absorption spectroscopy also reveal that the stacking sequence significantly modulates the electronic structures of few-layer graphene.[18, 131] AB-stacked and ABC-stacked graphene exhibit distinct properties in optical conductivity,[18] as shown in Figure 11b. The AB-stacked graphene exhibited weak, broadened absorption peaks, mainly at 0.24 eV and 0.58 eV, which arise from step-like van Hove singularities characteristic (Figure 11c).[132] The absorption peaks of ABC-stacked graphene show stronger absorption peaks at 0.26 eV and 0.35 eV, which are associated with 1D-like van Hove singularities (Figure 11d).[133] These van Hove singularities result from the energy extrema deviating from the K point due to the lower crystallographic symmetry.

The electronic properties of bilayer and multilayer graphene can be effectively modulated through various experimental approaches. Ohta et al.[130] tuned the carrier concentration in BLG through the deposition of K atoms, realized the opening, closing and re-opening of the energy gap, as shown in Figure 11e. Additionally, investigations on metal-induced layer exchange-synthesized highly conductive (2700 S cm^{-1}) multilayer graphene demonstrate the potential in electronics.[134] The development of multilayer graphene epidermal electronic skins based on laser scribed graphene further highlights promising applications in physiological signal monitoring.[27] Current progress of precise control of multilayer graphene stacking reveals its impact on

Table 3. Types of graphene based superatomic structures, synthesis or simulation methods, key electronic properties, and references.

Superatomic structure		Synthesis/Simulation approach	Key electronic property changes	Refs.
Magic-Angle Twisted Graphene	Magic-angle twisted bilayer graphene	Tear-and-stack dry-transfer technique, controlled twist angle (≈1.1°)	Flat bands near Fermi level, strong electron interactions, correlated insulator states, superconductivity	[24, 116, 15, 117, 118]
		Encapsulated in hBN, electrostatic gating	Mott-like insulator behavior at half-filling, reduced Fermi velocity, flat bands with high density of states	[116, 15, 117, 118]
		Tear-and-stack method, alignment with hBN substrate	Emergent ferromagnetism at 3/4 filling, giant anomalous Hall effect	[118]
		Encapsulated in hBN, electrostatic doping	Superconductivity with T_c up to 1.7 K, small Fermi surfaces near correlated insulator states	[15, 117, 118]
		"Tearing" method	Two distinct van Hove singularities, energy separation decreases with twist angle, correlation-induced gap at half-filling	[117]
	Twisted Double Bilayer Graphene	Tear and stack method with Bernal-stacked bilayer graphene twisted at small angles (e.g., 1.23°, 1.09°, 0.84°)	Tunable correlated insulator states, spin-polarized phases, flat bands near charge neutrality,	[125]
		Tear and stack method with Bernal-stacked bilayer graphene twisted at angles (e.g., 1.26°, 1.33°)	Flat bands tunable by electric fields, correlated insulator states at half- and quarter-fillings,	[125]
	Magic-Angle Multilayer Graphene (MATTG, MAT4G, MAT5G)	Alternating twist method with multilayer graphene (e.g., 3, 4, 5 layers)	Flat bands, robust superconductivity, Pauli limit violation	[126]
Multilayer graphene stacked structure	Multilayer graphene	Ni-induced layer exchange at 800 °C	High electrical conductivity (2700 S/cm), carrier mobility (550 $cm^2\ V^{-1}s^{-1}$)	[134]
	AB-stacked graphene multilayers with mirror plane symmetry	Tight-binding approach	Dirac fermions present in odd-numbered layers; normal fermions with parabolic dispersion in even-numbered layers	[128]
	ABC, ABA, ABCA, ABCC, ABAB stacking	Combination of the tight-binding approach and the self-consistent Hartree approximation	Band gap tuning with electric field; ABC stacking shows larger band gap than ABA stacking	[127]

electronic properties with tunable bandgap and highlights its potential in electronic devices, thermal conduction and nanoelectronics.

5. Summary and Outlook

5.1. Summary

This short review provides a brief introduction to the electronic properties of carbon-based materials, starting from graphite and diamond, and extending to superatomic structures constructed from nano units as fundamental building blocks. To facilitate comparative analysis, we have compiled key parameters including synthesis methods and electronic property changes, as shown in **Tables** 1–3. By reviewing the electronic characteristics of carbons across various dimensionalities, we wish to emphasize the potential of superatomic carbons in electronic devices.

5.2. Challenges

Despite remarkable progress in carbon-based structures and their superatomic assemblies, significant challenges remain at every stage, from fundamental understanding to synthesis and industrial application. In fundamental research, the mechanistic understanding of the dynamics for assembly is unclear, particularly in the preparation of fullerene polymers and covalently connected CNT architectures, impeding the precise control and optimization of properties. The characterization of high-pressure polymerization has technical limitations, preventing real-time monitoring of fullerene and CNT polymerization under extreme conditions, obscuring the comprehensive elucidation of topological bonding pathways involved in these structural transformations. Additionally, achieving multiscale electronic property modulation, ranging from quantum effects in individual nanotubes to macroscopic array synergies, requires more intensive theoretical and experimental investigations to enhance carrier mobility and optimize the integration density of devices.

Further into the atomic level, the challenge in precise control of superatomic structures originates from the complex bonding nature of carbon, often leading to byproducts or defects. Scalability remains a challenge, as synthesis methods like CVD for graphene often face trade-offs between scale and material quality/uniformity. Economic barriers stem from multiple factors including the need for ultra-pure precursors, specialized equipment requirements, and energy-intensive processing conditions

– particularly evident in SWNT manufacturing where catalyst costs and purification steps dominate. Meanwhile, environmental sustainability is another concern, as many synthesis protocols rely on hazardous chemicals like strong acids or generate significant carbon emissions.

Furthermore, there is a notable gap between laboratory research and industrial applications. Standardized protocols are needed to ensure reproducibility and consistency in material properties. Integrating superatomic structures into existing manufacturing processes and devices also presents technical challenges. Long-term stability and performance data under real-world conditions are still lacking.

5.3. Outlook

In observation of the challenges mentioned above, significant breakthroughs in both theoretical and experimental research are expected. By continuously optimizing the synthesis methods and characterization techniques, and integrating theoretical predictions with experimental validation, future research is expected to achieve major breakthroughs in wafer-scale carbon-based superatomic structures, unlocking new functionalities. These advancements are poised to revolutionize the science and technology of carbon materials, enabling the development of next-generation electronic, optoelectronic and energy-related applications based on such new carbons.

Advanced characterization techniques, including in situ and operando methods, would provide deeper insights into the mechanism of these materials, enabling precise control over their structures and properties. Sustainable synthesis methods using green chemistry and renewable resources will address environmental concerns and improve cost-effectiveness, facilitating widespread adoption. Data-driven methods such as machine learning (ML) and artificial intelligence will also play a transformative role. ML can predict material properties, guide experimental synthesis, and optimize design, thereby overcoming current challenges. For example, the deep-learning DFT Hamiltonian method,[135] which employs message-passing neural networks to learn DFT Hamiltonians, can achieve precise predictions of band structures, density of states, and optical properties with errors as low as the millielectronvolt level. With the development of transferable ML models and their integration with experimental technologies, the study of superatomic crystals is expected to enter a new stage of development.

The future of carbon-based superatomic structures is promising. Interdisciplinary approaches and technological innovations will drive the field forward, unlocking the full potential of these materials and ushering in a new era of advanced materials science and technology.

Acknowledgements

This work was supported by the National Natural Science Foundation of China (Nos. 52273234, 52325202); the Fundamental Research Funds for the Central Universities (WK2060000098, WK9990000170) and the open research fund of State Key Laboratory of Precision and Intelligent Chemistry (KY2490000300). The Supercomputing Center of USTC and the Hefei Advanced Computing Center are appreciated.

Conflict of Interest

The authors declare no conflict of interest.

Keywords

carbon nanotubes, carbon-based materials, electronic properties, fullerenes, graphene, superatomic crystals

Received: March 31, 2025
Revised: June 24, 2025

---

[1] H. W. Kroto, J. R. Heath, S. C. O'Brien, R. F. Curl, R. E. Smalley, *Nature* **1985**, *318*, 162.
[2] S. Iijima, *Nature* **1991**, *354*, 56.
[3] K. S. Novoselov, A. K. Geim, S. V. Morozov, D. Jiang, Y. Zhang, S. V. Dubonos, I. V. Grigorieva, A. A. Firsov, *Science* **2004**, *306*, 666.
[4] G. Li, Y. Li, H. Liu, Y. Guo, Y. Li, D. Zhu, *Chem. Commun.* **2010**, *46*, 3256.
[5] a) M. Yudasaka, S. Iijima, V. H. Crespi, in *Carbon Nanotubes: Advanced Topics in the Synthesis, Structure, Properties and Applications*, (Eds: A. Jorio, G. Dresselhaus, M. S. Dresselhaus), Springer Berlin Heidelberg, Berlin, Heidelberg **2008**, p. 605; b) S. Noriaki, *J. Phys. D: Appl. Phys.* **2004**, *37*, L17.
[6] O. Mykhailiv, H. Zubyk, M. E. Plonska-Brzezinska, *Inorg. Chim. Acta* **2017**, *468*, 49.
[7] a) D. Imoto, A. Yagi, K. Itami, *Precis. Chem.* **2023**, *1*, 516; b) Y. Zhang, D. Yang, S. H. Pun, H. Chen, Q. Miao, *Precis. Chem.* **2023**, *1*, 107; c) L. Zoppi, L. Martin-Samos, K. K. Baldridge, *Phys. Chem. Chem. Phys.* **2015**, *17*, 6114.
[8] J. Zhao, M. Feng, J. Yang, H. Petek, *ACS Nano* **2009**, *3*, 853.
[9] A. Takakura, K. Beppu, T. Nishihara, A. Fukui, T. Kozeki, T. Namazu, Y. Miyauchi, K. Itami, *Nature Communications* **2019**, *10*, 3040.
[10] A. H. Castro Neto, F. Guinea, N. M. R. Peres, K. S. Novoselov, A. K. Geim, *Rev. Mod. Phys.* **2009**, *81*, 109.
[11] R. E. Leuchtner, A. C. Harms, A. W. Castleman, Jr., *J. Chem. Phys.* **1989**, *91*, 2753.
[12] S. N. Khanna, P. Jena, *Phys. Rev. B* **1995**, *51*, 13705.
[13] J. L. Martins, R. Car, J. Buttet, *Surf. Sci.* **1981**, *106*, 265.
[14] M. Feng, J. Zhao, H. Petek, *Science* **2008**, *320*, 359.
[15] Y. Cao, V. Fatemi, S. Fang, K. Watanabe, T. Taniguchi, E. Kaxiras, P. Jarillo-Herrero, *Nature* **2018**, *556*, 43.
[16] J. Liu, N. P. Wickramaratne, S. Z. Qiao, M. Jaroniec, *Nat. Mater.* **2015**, *14*, 763.
[17] J. Laranjeira, L. Marques, *Mater. Today Commun.* **2020**, *23*, 100906.
[18] K. F. Mak, J. Shan, T. F. Heinz, *Phys. Rev. Lett.* **2010**, *104*, 176404.
[19] a) A. A. Avetisyan, B. Partoens, F. M. Peeters, *Phys. Rev. B* **2009**, *79*, 035421; b) B. Wang, Y. Ma, N. Li, Y. Wu, F. Li, Y. Chen, *Adv. Mater.* **2010**, *22*, 3067.
[20] C. Pei, L. Wang, *Matter Radiat. Extremes* **2019**, *4*, 028201.
[21] H. Li, B. C. K. Tee, J. J. Cha, Y. Cui, J. W. Chung, S. Y. Lee, Z. Bao, *J. Am. Chem. Soc.* **2012**, *134*, 2760.
[22] H. Shi, L. Ding, D. Zhong, J. Han, L. Liu, L. Xu, P. Sun, H. Wang, J. Zhou, L. Fang, Z. Zhang, L.-M. Peng, *Nat. Electron.* **2021**, *4*, 405.
[23] Z. Zhang, Y. Chen, P. Shen, J. Chen, S. Wang, B. Wang, S. Ma, B. Lyu, X. Zhou, S. Lou, Z. Wu, Y. Xie, C. Zhang, L. Wang, K. Xu, H. Li, G. Wang, K. Watanabe, T. Taniguchi, D. Qian, J. Jia, Q. Liang, X. Wang, W. Yang, G. Zhang, C. Jin, W. Ouyang, Z. Shi, *Science* **2025**, *387*, 1310.

[24] D. Rodan-Legrain, Y. Cao, J. M. Park, S. C. de la Barrera, M. T. Randeria, K. Watanabe, T. Taniguchi, P. Jarillo-Herrero, *Nat. Nanotechnol.* **2021**, *16*, 769.
[25] T. Wang, L. Zhang, J. Wu, M. Chen, S. Yang, Y. Lu, P. Du, *Angew. Chem., Int. Ed.* **2023**, *62*, 202311352.
[26] R. Zhang, Y. Zhang, F. Wei, *Chem. Soc. Rev.* **2017**, *46*, 3661.
[27] Y. Qiao, Y. Wang, H. Tian, M. Li, J. Jian, Y. Wei, Y. Tian, D.-Y. Wang, Y. Pang, X. Geng, X. Wang, Y. Zhao, H. Wang, N. Deng, M. Jian, Y. Zhang, R. Liang, Y. Yang, T.-L. Ren, *ACS Nano* **2018**, *12*, 8839.
[28] P. R. Wallace, *Phys. Rev.* **1947**, *71*, 622.
[29] B. Partoens, F. M. Peeters, *Phys. Rev. B* **2006**, *74*, 075404.
[30] S. Latil, L. Henrard, *Phys. Rev. Lett.* **2006**, *97*, 036803.
[31] B. Dawson, W. Cochran, *Proc. R. Soc. London, Ser. A* **1967**, *298*, 264.
[32] C. A. Klein, G. F. Cardinale, *Diamond Relat. Mater.* **1993**, *2*, 918.
[33] C. D. Clark, P. J. Dean, P. V. Harris, W. C. Price, *Proc. R. Soc. London, Ser. A* **1964**, *277*, 312.
[34] E. A. Ekimov, V. A. Sidorov, E. D. Bauer, N. N. Mel'nik, N. J. Curro, J. D. Thompson, S. M. Stishov, *Nature* **2004**, *428*, 542.
[35] L. Wei, P. K. Kuo, R. L. Thomas, T. R. Anthony, W. F. Banholzer, *Phys. Rev. Lett.* **1993**, *70*, 3764.
[36] C. E. Nebel, in *Nanodiamonds* (Ed: J.-C. Arnault), Elsevier, Amsterdam **2017**, p. 1.
[37] H. Park, J. Park, A. K. L. Lim, E. H. Anderson, A. P. Alivisatos, P. L. McEuen, *Nature* **2000**, *407*, 57.
[38] S. Chaudhury, S. K. Sinha, in *Nanoelectronics* (Ed: B. K. Kaushik), Elsevier, Amsterdam **2019**, p. 375.
[39] J. H. Weaver, J. L. Martins, T. Komeda, Y. Chen, T. R. Ohno, G. H. Kroll, N. Troullier, R. E. Haufler, R. E. Smalley, *Phys. Rev. Lett.* **1991**, *66*, 1741.
[40] M. Bühl, A. Hirsch, *Chem. Rev.* **2001**, *101*, 1153.
[41] W. H. Green, S. M. Gorun, G. Fitzgerald, P. W. Fowler, A. Ceulemans, B. C. Titeca, *J. Phys. Chem.* **1996**, *100*, 14892.
[42] R. C. Haddon, R. E. Palmer, H. W. Kroto, P. A. Sermon, H. W. Kroto, A. L. Mackay, G. Turner, D. R. M. Walton, *Phys. Eng. Sci.* **1993**, *343*, 53.
[43] J. O. Johansson, G. G. Henderson, F. Remacle, E. E. B. Campbell, *Phys. Rev. Lett.* **2012**, 108.
[44] E. Bohl, K. P. Sokół, B. Mignolet, J. O. F. Thompson, J. O. Johansson, F. Remacle, E. E. B. Campbell, *J. Phys. Chem. A* **2015**, *119*, 11504.
[45] T. W. Ebbesen, H. J. Lezec, H. Hiura, J. W. Bennett, H. F. Ghaemi, T. Thio, *Nature* **1996**, *382*, 54.
[46] T. W. Odom, J.-L. Huang, P. Kim, C. M. Lieber, *Nature* **1998**, *391*, 62.
[47] C. L. Kane, E. J. Mele, *Phys. Rev. Lett.* **1997**, *78*, 1932.
[48] E. A. Laird, F. Kuemmeth, G. A. Steele, K. Grove-Rasmussen, J. Nygård, K. Flensberg, L. P. Kouwenhoven, *Rev. Mod. Phys.* **2015**, *87*, 703.
[49] T. Dürkop, S. A. Getty, E. Cobas, M. S. Fuhrer, *Nano Lett.* **2004**, *4*, 35.
[50] a) C. Jianwei, Ç. Tahir, A. G. William, III, *Nanotechnology* **2000**, *11*, 65; b) S. Berber, Y.-K. Kwon, D. Tománek, *Phys. Rev. Lett.* **2000**, *84*, 4613.
[51] K. I. Bolotin, K. J. Sikes, Z. Jiang, M. Klima, G. Fudenberg, J. Hone, P. Kim, H. L. Stormer, *Solid State Commun.* **2008**, *146*, 351.
[52] a) Y. Zhang, Y.-W. Tan, H. L. Stormer, P. Kim, *Nature* **2005**, *438*, 201; b) K. S. Novoselov, Z. Jiang, Y. Zhang, S. V. Morozov, H. L. Stormer, U. Zeitler, J. C. Maan, G. S. Boebinger, P. Kim, A. K. Geim, *Science* **2007**, *315*, 1379.
[53] F. Schwierz, *Nat. Nanotechnol.* **2010**, *5*, 487.
[54] A. A. Balandin, S. Ghosh, W. Bao, I. Calizo, D. Teweldebrhan, F. Miao, C. N. Lau, *Nano Lett.* **2008**, *8*, 902.
[55] a) L. K. Shrestha, Q. Ji, T. Mori, K. i. Miyazawa, Y. Yamauchi, J. P. Hill, K. Ariga, *Chem. - Asian J.* **2013**, *8*, 1662; b) R. A. Rakkesh, P. N. B. Rebecca, T. B. Naveen, D. Durgalakshmi, S. Balakumar, *Part. Part. Syst. Charact.* **2023**, *41*, 2300125; c) A. L. Elías, N. Perea-López, L. P. Rajukumar, A. McCreary, F. López-Urías, H. Terrones, M. Terrones, in *Nanotube Superfiber Materials*, (Eds: M. J. Schulz, V. N. Shanov, Z. Yin), William Andrew Publishing, Boston, MA **2014**, pp.457-493; d) Y. Zhang, F. Pan, K. Ni, Y. Zhu, *Natl. Sci. Rev.* **2025**, *12*, nwaf125; e) S. Xie, K. Ni, Y. Zhu, *Precis. Chem.* **2025**.
[56] X.-D. Xiang, J. G. Hou, G. Briceño, W. A. Vareka, R. Mostovoy, A. Zettl, V. H. Crespi, M. L. Cohen, *Science* **1992**, *256*, 1190.
[57] R. W. Lof, M. A. van Veenendaal, B. Koopmans, H. T. Jonkman, G. A. Sawatzky, *Phys. Rev. Lett.* **1992**, *68*, 3924.
[58] P. J. F. Harris, *C-J. Carbon Res.* **2020**, *6*, 71.
[59] K. Miyazawa, Y. Kuwasaki, K. Hamamoto, S. Nagata, A. Obayashi, M. Kuwabara, *Surf. Interface Anal.* **2003**, *35*, 117.
[60] Y. G. Guo, C. J. Li, L. J. Wan, D. M. Chen, C. R. Wang, C. L. Bai, Y. G. Wang, *Adv. Funct. Mater.* **2003**, *13*, 626.
[61] Z. Lu, W. Deng, X. Fang, J. Xiao, B. Lu, X. Zhang, A. A. A. Pirzado, J. Jie, X. Zhang, *Adv. Funct. Mater.* **2021**, *31*, 2105459.
[62] S. Kobayashi, T. Takenobu, S. Mori, A. Fujiwara, Y. Iwasa, *Sci. Technol. Adv. Mater.* **2003**, *4*, 371.
[63] X. Chen, S. Yamanaka, *Chem. Phys. Lett.* **2002**, *360*, 501.
[64] X. Chen, S. Yamanaka, K. Sako, Y. Inoue, M. Yasukawa, *Chem. Phys. Lett.* **2002**, *356*, 291.
[65] L. Hou, X. Cui, B. Guan, S. Wang, R. Li, Y. Liu, D. Zhu, J. Zheng, *Nature* **2022**, *606*, 507.
[66] E. Meirzadeh, A. M. Evans, M. Rezaee, M. Milich, C. J. Dionne, T. P. Darlington, S. T. Bao, A. K. Bartholomew, T. Handa, D. J. Rizzo, R. A. Wiscons, M. Reza, A. Zangiabadi, N. Fardian-Melamed, A. C. Crowther, P. J. Schuck, D. N. Basov, X. Zhu, A. Giri, P. E. Hopkins, P. Kim, M. L. Steigerwald, J. Yang, C. Nuckolls, X. Roy, *Nature* **2023**, *613*, 71.
[67] X.-K. Zhao, Y.-Y. Zhang, J. Zhao, H.-S. Hu, J. Li, *Inorg. Chem.* **2024**, *63*, 11572.
[68] C. H. Xu, G. E. Scuseria, *Phys. Rev. Lett.* **1995**, *74*, 274.
[69] Y. Iwasa, T. Arima, R. M. Fleming, T. Siegrist, O. Zhou, R. C. Haddon, L. J. Rothberg, K. B. Lyons, H. L. Carter, A. F. Hebard, R. Tycko, G. Dabbagh, J. J. Krajewski, G. A. Thomas, T. Yagi, *Science* **1994**, *264*, 1570.
[70] L. Yu, J. Xu, B. Peng, G. Qin, G. Su, *J. Phys. Chem. Lett.* **2022**, *13*, 11622.
[71] X. Cui, D. Han, H. Guo, L. Zhou, J. Qiao, Q. Liu, Z. Cui, Y. Li, C. Lin, L. Cao, W. Ji, H. Petek, M. Feng, *Nat. Commun.* **2019**, *10*, 3374.
[72] M. Núñez-Regueiro, L. Marques, J. L. Hodeau, O. Béthoux, M. Perroux, *Phys. Rev. Lett.* **1995**, *74*, 278.
[73] T. Miyake, S. Saito, *Chem. Phys. Lett.* **2003**, *380*, 589.
[74] S. Yamanaka, A. Kubo, K. Inumaru, K. Komaguchi, N. S. Kini, T. Inoue, T. Irifune, *Phys. Rev. Lett.* **2006**, *96*, 076602.
[75] S. Okada, S. Saito, A. Oshiyama, *Phys. Rev. Lett.* **1999**, *83*, 1986.
[76] B. Mortazavi, *Carbon* **2023**, *213*, 118293.
[77] F. Pan, K. Ni, T. Xu, H. Chen, Y. Wang, K. Gong, C. Liu, X. Li, M.-L. Lin, S. Li, X. Wang, W. Yan, W. Yin, P.-H. Tan, L. Sun, D. Yu, R. S. Ruoff, Y. Zhu, *Nature* **2023**, *614*, 95.
[78] K. Ni, F. Pan, Y. Zhu, *Adv. Funct. Mater.* **2022**, *32*, 2203894.
[79] J. P. Perdew, M. Levy, *Phys. Rev. Lett.* **1983**, *51*, 1884.
[80] A. V. Krukau, O. A. Vydrov, A. F. Izmaylov, G. E. Scuseria, *J. Chem. Phys.* **2006**, *125*.
[81] M. Shishkin, G. Kresse, *Phys. Rev. B* **2007**, *75*, 235102.
[82] A. F. Hebard, M. J. Rosseinsky, R. C. Haddon, D. W. Murphy, S. H. Glarum, T. T. M. Palstra, A. P. Ramirez, A. R. Kortan, *Nature* **1991**, *350*, 600.
[83] A. F. Hebard, *Phys. Today* **1992**, *45*, 26.
[84] a) S. Pekker, A. Jánossy, L. Mihaly, O. Chauvet, M. Carrard, L. Forró, *Science* **1994**, *265*, 1077; b) P. W. Stephens, G. Bortel, G. Faigel, M.

Tegze, A. Jánossy, S. Pekker, G. Oszlanyi, L. Forró, *Nature* **1994**, *370*, 636.

[85] a) O. Zhou, J. E. Fischer, N. Coustel, S. Kycia, Q. Zhu, A. R. McGhie, W. J. Romanow, J. P. McCauley, A. B. Smith, D. E. Cox, *Nature* **1991**, *351*, 462; b) W. Andreoni, **2012**.

[86] R. C. Haddon, *Acc. Chem. Res.* **1992**, *25*, 127.

[87] R. C. Haddon, A. F. Hebard, M. J. Rosseinsky, D. W. Murphy, S. J. Duclos, K. B. Lyons, B. Miller, J. M. Rosamilia, R. M. Fleming, A. R. Kortan, S. H. Glarum, A. V. Makhija, A. J. Muller, R. H. Eick, S. M. Zahurak, R. Tycko, G. Dabbagh, F. A. Thiel, *Nature* **1991**, *350*, 320.

[88] E. Wang, J. D. Adelinia, M. Chavez-Cervantes, T. Matsuyama, M. Fechner, M. Buzzi, G. Meier, A. Cavalleri, *Nat. Commun.* **2023**, *14*, 7233.

[89] A. Oshiyama, S. Saito, N. Hamada, Y. Miyamoto, *J. Phys. Chem. Solids* **1992**, *53*, 1457.

[90] K. Tanigaki, T. W. Ebbesen, S. Saito, J. Mizuki, J. S. Tsai, Y. Kubo, S. Kuroshima, *Nature* **1991**, *352*, 222.

[91] M. J. Rosseinsky, A. P. Ramirez, S. H. Glarum, D. W. Murphy, R. C. Haddon, A. F. Hebard, T. T. M. Palstra, A. R. Kortan, S. M. Zahurak, A. V. Makhija, *Phys. Rev. Lett.* **1991**, *66*, 2830.

[92] O. Zhou, Q. Zhu, J. E. Fischer, N. Coustel, G. B. M. Vaughan, P. A. Heiney, J. P. McCauley, A. B. Smith, *Science* **1992**, *255*, 833.

[93] A. R. Kortan, N. Kopylov, S. Glarum, E. M. Gyorgy, A. P. Ramirez, R. M. Fleming, F. A. Thiel, R. C. Haddon, *Nature* **1992**, *355*, 529.

[94] A. R. Kortan, N. Kopylov, S. Glarum, E. M. Gyorgy, A. P. Ramirez, R. M. Fleming, O. Zhou, F. A. Thiel, P. L. Trevor, R. C. Haddon, *Nature* **1992**, *360*, 566.

[95] a) D.-M. Tang, O. Cretu, S. Ishihara, Y. Zheng, K. Otsuka, R. Xiang, S. Maruyama, H.-M. Cheng, C. Liu, D. Golberg, *Nat. Rev. Electr. Eng.* **2024**, *1*, 149; b) F. Yang, M. Wang, D. Zhang, J. Yang, M. Zheng, Y. Li, *Chem. Rev.* **2020**, *120*, 2693.

[96] L. Liu, J. Han, L. Xu, J. Zhou, C. Zhao, S. Ding, H. Shi, M. Xiao, L. Ding, Z. Ma, C. Jin, Z. Zhang, L.-M. Peng, *Science* **2020**, *368*, 850.

[97] K. R. Jinkins, S. M. Foradori, V. Saraswat, R. M. Jacobberger, J. H. Dwyer, P. Gopalan, A. Berson, M. S. Arnold, *Sci. Adv.* **2021**, *7*, abh0640.

[98] J. Wang, X. Jin, Z. Liu, G. Yu, Q. Ji, H. Wei, J. Zhang, K. Zhang, D. Li, Z. Yuan, J. Li, P. Liu, Y. Wu, Y. Wei, J. Wang, Q. Li, L. Zhang, J. Kong, S. Fan, K. Jiang, *Nat. Catal.* **2018**, *1*, 326.

[99] F. Yang, X. Wang, J. Si, X. Zhao, K. Qi, C. Jin, Z. Zhang, M. Li, D. Zhang, J. Yang, Z. Zhang, Z. Xu, L.-M. Peng, X. Bai, Y. Li, *ACS Nano* **2017**, *11*, 186.

[100] a) Q. Cao, S.-J. Han, G. S. Tulevski, Y. Zhu, D. D. Lu, W. Haensch, *Nat. Nanotechnol.* **2013**, *8*, 180; b) S. W. Hong, T. Banks, J. A. Rogers, *Adv. Mater.* **2010**, *22*, 1826; c) G. J. Brady, Y. Joo, M.-Y. Wu, M. J. Shea, P. Gopalan, M. S. Arnold, *ACS Nano* **2014**, *8*, 11614; d) S. Shekhar, P. Stokes, S. I. Khondaker, *ACS Nano* **2011**, *5*, 1739.

[101] J. Si, D. Zhong, H. Xu, M. Xiao, C. Yu, Z. Zhang, L.-M. Peng, *ACS Nano* **2018**, *12*, 627.

[102] S. Zhang, N. Nguyen, B. Leonhardt, C. Jolowsky, A. Hao, J. G. Park, R. Liang, *Adv. Electron. Mater.* **2019**, *5*, 1800811.

[103] a) S. Zhang, L. Kang, X. Wang, L. Tong, L. Yang, Z. Wang, K. Qi, S. Deng, Q. Li, X. Bai, F. Ding, J. Zhang, *Nature* **2017**, *543*, 234; b) M. M. Shulaker, G. Pitner, G. Hills, M. Giachino, H. S. P. Wong, S. Mitra, presented at 2014 IEEE International Electron Devices Meeting 15–17 Dec. 2014, **2014**.

[104] M. Terrones, F. Banhart, N. Grobert, J. C. Charlier, H. Terrones, P. M. Ajayan, *Phys. Rev. Lett.* **2002**, *89*, 075505.

[105] D. C. Wei, L. C. Cao, L. Fu, X. L. Li, Y. Wang, G. Yu, Y. Q. Liu, *Adv. Mater.* **2007**, *19*, 386.

[106] Z. Yao, H. W. C. Postma, L. Balents, C. Dekker, *Nature* **1999**, *402*, 273.

[107] M. Bockrath, D. H. Cobden, J. Lu, A. G. Rinzler, R. E. Smalley, L. Balents, P. L. McEuen, *Nature* **1999**, *397*, 598.

[108] D. Wei, Y. Liu, *Adv. Mater.* **2008**, *20*, 2815.

[109] R. Zhou, R. Liu, L. Li, X. Wu, X. C. Zeng, *J. Phys. Chem. C* **2011**, *115*, 18174.

[110] V. R. Coluci, D. S. Galvão, A. Jorio, *Nanotechnology* **2006**, *17*, 617.

[111] G. Treboux, P. Lapstun, K. Silverbrook, *Chem. Phys. Lett.* **1999**, *306*, 402.

[112] V. Meunier, M. B. Nardelli, J. Bernholc, T. Zacharia, J.-C. Charlier, *Appl. Phys. Lett.* **2002**, *81*, 5234.

[113] M. Menon, D. Srivastava, *Phys. Rev. Lett.* **1997**, *79*, 4453.

[114] M. Wang, W. Shan, H. Wang, *Phys. Status Solidi* **2023**, *260*, 2200344.

[115] a) Y. Cao, J. Y. Luo, V. Fatemi, S. Fang, J. D. Sanchez-Yamagishi, K. Watanabe, T. Taniguchi, E. Kaxiras, P. Jarillo-Herrero, *Phys. Rev. Lett.* **2016**, *117*, 116804; b) K. Kim, M. Yankowitz, B. Fallahazad, S. Kang, H. C. P. Movva, S. Huang, S. Larentis, C. M. Corbet, T. Taniguchi, K. Watanabe, S. K. Banerjee, B. J. LeRoy, E. Tutuc, *Nano Lett.* **2016**, *16*, 1989.

[116] Y. Cao, V. Fatemi, A. Demir, S. Fang, S. L. Tomarken, J. Y. Luo, J. D. Sanchez-Yamagishi, K. Watanabe, T. Taniguchi, E. Kaxiras, R. C. Ashoori, P. Jarillo-Herrero, *Nature* **2018**, *556*, 80.

[117] A. Kerelsky, L. J. McGilly, D. M. Kennes, L. Xian, M. Yankowitz, S. Chen, K. Watanabe, T. Taniguchi, J. Hone, C. Dean, A. Rubio, A. N. Pasupathy, *Nature* **2019**, *572*, 95.

[118] a) A. L. Sharpe, E. J. Fox, A. W. Barnard, J. Finney, K. Watanabe, T. Taniguchi, M. A. Kastner, D. Goldhaber-Gordon, *Science* **2019**, *365*, 605; b) J. H. Pixley, E. Y. Andrei, *Science* **2019**, *365*, 543.

[119] M. Yankowitz, S. Chen, H. Polshyn, Y. Zhang, K. Watanabe, T. Taniguchi, D. Graf, A. F. Young, C. R. Dean, *Science* **2019**, *363*, 1059.

[120] M. Xie, A. H. MacDonald, *Phys. Rev. Lett.* **2020**, *124*, 097601.

[121] S. Lisi, X. Lu, T. Benschop, T. A. de Jong, P. Stepanov, J. R. Duran, F. Margot, I. Cucchi, E. Cappelli, A. Hunter, A. Tamai, V. Kandyba, A. Giampietri, A. Barinov, J. Jobst, V. Stalman, M. Leeuwenhoek, K. Watanabe, T. Taniguchi, L. Rademaker, S. J. van der Molen, M. P. Allan, D. K. Efetov, F. Baumberger, *Nat. Phys.* **2021**, *17*, 189.

[122] D. Wong, K. P. Nuckolls, M. Oh, B. Lian, Y. Xie, S. Jeon, K. Watanabe, T. Taniguchi, B. A. Bernevig, A. Yazdani, *Nature* **2020**, *582*, 198.

[123] P. Stepanov, I. Das, X. Lu, A. Fahimniya, K. Watanabe, T. Taniguchi, F. H. L. Koppens, J. Lischner, L. Levitov, D. K. Efetov, *Nature* **2020**, *583*, 375.

[124] L. Ge, K. Ni, X. Wu, Z. Fu, Y. Lu, Y. Zhu, *Nanoscale* **2021**, *13*, 9264.

[125] a) Y. Cao, D. Rodan-Legrain, O. Rubies-Bigorda, J. M. Park, K. Watanabe, T. Taniguchi, P. Jarillo-Herrero, *Nature* **2020**, *583*, 215; b) X. Liu, Z. Hao, E. Khalaf, J. Y. Lee, Y. Ronen, H. Yoo, D. Haei Najafabadi, K. Watanabe, T. Taniguchi, A. Vishwanath, P. Kim, *Nature* **2020**, *583*, 221.

[126] J. M. Park, Y. Cao, L.-Q. Xia, S. Sun, K. Watanabe, T. Taniguchi, P. Jarillo-Herrero, *Nat. Mater.* **2022**, *21*, 877.

[127] A. A. Avetisyan, B. Partoens, F. M. Peeters, *Phys. Rev. B* **2010**, *81*, 115432.

[128] B. Partoens, F. M. Peeters, *Phys. Rev. B* **2007**, 75.

[129] H. Min, A. H. MacDonald, *Phys. Rev. B* **2008**, *77*, 155416.

[130] T. Ohta, A. Bostwick, T. Seyller, K. Horn, E. Rotenberg, *Science* **2006**, *313*, 951.

[131] Y. Hao, Y. Wang, L. Wang, Z. Ni, Z. Wang, R. Wang, C. K. Koo, Z. Shen, J. T. L. Thong, *Small* **2010**, *6*, 195.

[132] F. Bassani, G. P. Parravicini, R. A. Ballinger, J. L. Birman, *Phys. Today* **1976**, *29*, 58.

[133] F. Guinea, A. H. Castro Neto, N. M. R. Peres, *Phys. Rev. B* **2006**, *73*, 245426.

[134] H. Murata, Y. Nakajima, N. Saitoh, N. Yoshizawa, T. Suemasu, K. Toko, *Sci. Rep.* **2019**, *9*, 4068.

[135] H. Li, Z. Wang, N. Zou, M. Ye, R. Xu, X. Gong, W. Duan, Y. Xu, *Nat. Comput. Sci.* **2022**, *2*, 367.

Shuqi Xie is a Ph.D. candidate in the Department of Materials Science and Engineering at the University of Science and Technology of China. She received her B.S. degree in Materials Science and Engineering from Nanchang Hangkong University in 2022. Her current research focuses on high-throughput property calculations and structure-property relationships for carbon materials.

Kun Ni is an associate research fellow in the Department of Materials Science and Engineering at the University of Science and Technology of China (USTC). He received his B.S. (2014) and Ph.D. (2019) degree from USTC, followed by postdoctoral research at the Hefei National Research Center for Physical Sciences at the Microscale, USTC. Since 2021, he has been a special associate researcher in the School of Chemistry and Materials Science, USTC. His research interests are the theoretical design and application of new materials using density functional theory combined with machine learning methods.

Yanwu Zhu is a professor in the Department of Materials Science and Engineering at the University of Science and Technology of China. He obtained his Ph.D. in Physics from the National University of Singapore in 2007, followed by postdoctoral research at National University of Singapore and the University of Texas at Austin. His research interests include preparation and characterization of novel carbon materials, especially the theoretical design, precise preparation, electrical characterization and device development of carbon-based superatomic crystals, as well as their applications in energy storage and conversion.